Automated Precision Three-Axis Scanner and Velocity Sensor for Laser Dermatology

by

Tang Yew Tan

M.Eng., Mechanical Engineering,
Imperial College of Science, Technology and Medicine, London, 1997

Submitted to the Department of Mechanical Engineering
in Partial Fulfillment of the Requirements for the Degree of

Master of Science in Mechanical Engineering

at the

Massachusetts Institute of Technology

January 1999

Signature of Author.....
Department of Mechanical Engineering
January 15, 1998

Certified by.....
Dr. Andre Sharon
Executive Officer of the Manufacturing Institute
Thesis Supervisor

Accepted By.....
Ain A. Sonin
Chairman, Department Committee on Graduate Studies

Automated Precision Three-Axis Scanner and Velocity Sensor for Laser Dermatology

by

Tang Yew Tan

Submitted to the Department of Mechanical Engineering
on January 15, 1999 in Partial Fulfillment of the
Requirements for the Degree of Master of Science in
Mechanical Engineering

ABSTRACT

Automated computer controlled systems are increasingly integrated into laser applications for the medical field. This helps improve system performance, which results in better surgical processes. Laser dermatology represents one of the new challenges in this field. The development of an automated precision three-axis scanner will help increase laser process throughput and consistency.

This dissertation describes the development of a computer controlled scanner for laser-based permanent hair removal. Clinical trials performed on the integrated scanner-laser system showed a faster application rate and better process consistency compared to the conventional manual technique. Tests also indicated that a better velocity sensor has to be developed to obtain actual relative velocity with respect to the skin. This would allow the scanner system parameters to be adjusted in real-time. The second phase of the dissertation describes the development of a velocity sensor that can cope with the elastic characteristic of human skin. Experiments were performed on contact and non-contact types of sensors and the results are discussed.

Thesis Supervisor: Dr. Andre Sharon
Title: Executive Office of the Manufacturing Institute Laboratory

Acknowledgement

Dr. Andre Sharon , for giving me the opportunity to work on the project and providing unconstrained guidance.

Dr.Altschuler, Paul , Rick and the Palomar team, for the help and inspiring ideas.

Min , I aspire to reach your state of intellectual nirvana. Am sure snowboarding regularly will help. Thanks for everything.

Sieu, for the joy and laughter, the food (even the hidden ones), the bucket of change, the bad taste in music and the inspiring thoughts.

Pankaj, for reminding me to take my meals and being a good buddy. Maybe next time I'll let you document my project.

Jason, for expanding the horizons in my mind. The 60's was in the past, but for someone who thinks fish is spelled with a 'ph', I'll let that pass.

Wayne, for the loan of your sports car, advice and interesting thoughts.

Dai, for the mental sparing and keeping me on my toes

Prakash, Brian and Mike, for taking entertainment to a new dimension.

Jamie, Amir and Fardad, for being great stress relievers and friends. Brady power!

Victor, for the smiles and cheerfulness that have helped a tremendous amount.

To all the other friends at MIT who have helped make this experience a memorable one.

My family and Celine, for the support, encouragement and love. I wouldn't have gone this far without the help.

1 Introduction

Automated computer controlled systems are increasingly integrated into generic appliances and sophisticated equipment, helping enhance and improve product performance. The spectrum of applications ranges from household washing machines to intelligent cruise missiles. Computers have increased in capacity and performance over the years making it possible to push the envelope in technological advancements. In the laser-medical field, various techniques such as laser pulsing, beam scanning and laser pulse generation rely on computer control. This has improved the overall performance of laser systems resulting in better surgical results. The applications of laser systems in medical surgery are wide and varied.

This dissertation presents the motivation of developing a versatile automated computer controlled machine specifically for laser dermatology applications. There are two main sections to this dissertation. The first section focuses on the development and design of a scanner for automating the laser hair removal process in dermatology applications. The second addresses the challenges and methodologies involved in developing a velocity sensor for the scanner that would provide actual relative velocity data between the skin and the laser hand piece.

Laser dermatology is a growing field and this chapter will provide a brief introduction to laser technology and the critical processes involved in laser-tissue interaction. Various laser systems used in the medical field will be briefly described as well as their application in laser dermatology.

1.1 Project Initiative

The potential market for laser dermatology applications exceeds $ 1 billion dollar in the United States. Apart from creating a product that has superior laser light properties for good photothermolysis performance, speed and reduced discomfort to the patient are the other important factors that would help determine the success of a laser product.

The MIT Manufacturing Institute (MIT/MI) scanner was developed to address the speed, consistency and comfort issues of the laser procedure. The scanner was designed to penetrate high-volume medical practices since both providers and consumers will benefit from dramatically improved speed, ease of use and reliability. The first prototype was designed to compliment the Palomar E2000^{TM} system. Palomar Medical Technologies, Inc. is a leading developer and supplier of proprietary laser systems for hair removal and other cosmetic laser treatments.

The development of an automated precision scanner helps control the laser process by creating a precise and reproducible operation. This machine is used to accurately position the laser hand piece at the desired location in minimum time. The machine also serves to automate tedious, repetitive and time-consuming processes. Laser hair removal was chosen as the dermatological process to be initially addressed as the current techniques are prone to positional error and tend to be very time consuming. Currently, an operator has to manually position and apply a firm force on the laser hand piece in small adjacent steps across a large skin surface. Most laser lenses have a spot size of approximately 10mm and a considerable time is required to process large patches of skin such as on the leg, thigh and back. Inaccurate positioning could also create zones of gross multi-overlapping that can cause epidermal injury.

1.2 Proposed Approach

In 1997, the MIT/MI proposed the development of a 'proof-of-concept' prototype precision scanner for laser dermatology applications that would have mass production potential. The prototype scanner would have to be flexible in both its mechanical design and user interface. Most of the working variables would be changed through software to facilitate the identification of the critical variables. The scanning quality of the laser beam in the operating field is not only a function of the planar displacement of the X-Y Axes, but also of the Z-axis. This necessitates precision motion of the laser scanner in all three-axes.

The initiative to investigate different and new velocity sensing mechanisms was motivated by the need to develop a simple and inexpensive method that can directly detect the relative velocity between the device and the skin surface. Skin has an elastic characteristic that could provide erroneous results with current velocity sensing methods available in the market.

1.3 Background on Laser Technology

Laser is the acronym for Light Amplification by Stimulated Emission of Radiation. Albert Einstein described the underlying principle of a laser in 1917 and the first practical demonstration took place in 1960 when Theodore Maiman successfully stimulated a ruby crystal to produce laser light of 690nm. Within a year, the use of lasers had expanded to include ophthalmology for photocoagulation. This set the stage for further development of other lasers working at different wavelengths. Today, the applications of lasers have increased tremendously and span almost every field of human endeavor.

Laser light is produced by the action of the excited state of a large population of atoms or molecules that have absorbed energy from an external source. The process begins with the spontaneous release of energy by a small amount of excited states, producing photons of light in the laser medium. These photons in turn initiate a chain reaction of identical photon emissions in other excited states that are encountered. This phenomenon of emissions is the underlying process that creates laser light.

Three properties of laser light (Figure 1.1) were recognized as extremely important:

a) The laser emits a collimated (parallel) beam of light. This enables high-powered applications and allows it to travel in a single direction with very little divergence over long distances. Ordinary light waves spread and lose intensity quickly.

b) The light is monochromatic, consisting of one color or a narrow range of colors. Ordinary light has a much wider range of wavelengths and colors

c) Laser light is coherent, which means all of the light waves move in phase together in both time and space.

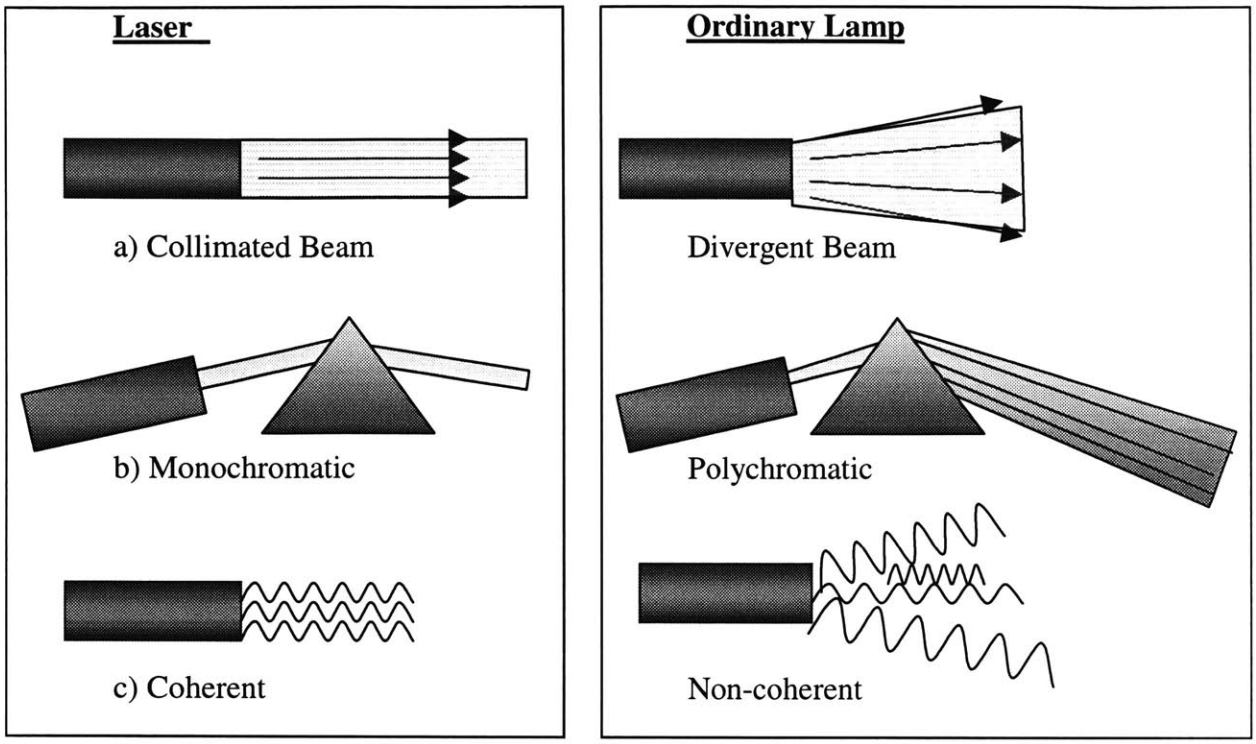

Figure 1.1 Comparison of a laser and an ordinary light source

1.4 Optical Properties of Tissue

The fundamentals of laser-tissue interaction are generally well understood with much active research currently conducted. There are four primary energy transfer mechanisms between laser and tissue: absorption, scattering, reflection and transmission. Energy conservation requires that the incident light energy: Ii = Ir + Is + Ia +It.

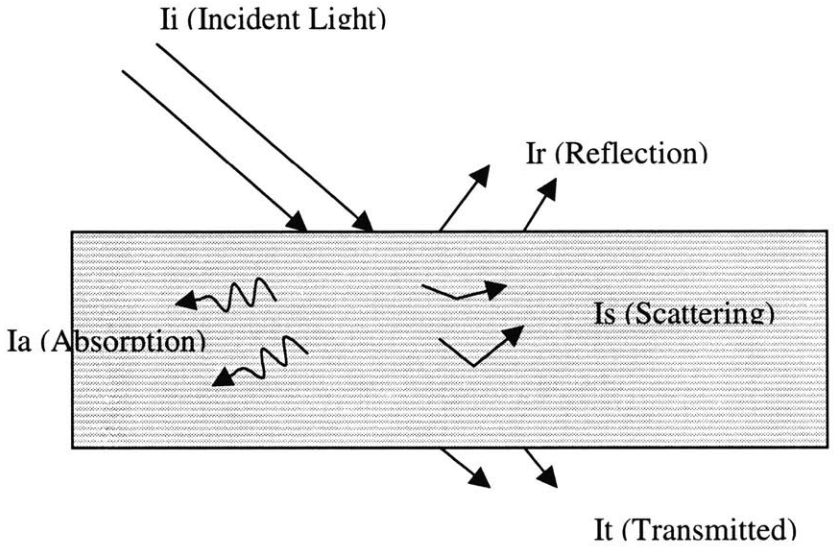

Figure 1.2 Spectral behavior of human skin, indicated is the residual intensity

1.4.1 Absorption

The two most important modes of light-tissue interaction during laser treatment are absorption and scattering. Absorption forms the dominant effect. When the high energy density laser beam is absorbed in living tissue, a rapid rise in temperature is caused. At low energy levels, the heat generated in the spot coagulates blood and causes homeostasis (arrest of blood flow) of small blood vessels. At higher levels, it causes ablation (vaporization) of tissue. Major clinical differences between surgical lasers arise from differences in absorption characteristics. The principal constituent of biological tissue is water. In adult humans, the average water content is about 70%. (Percentage varies with

age). The remainder consists mainly of organic molecules such as hemoglobin, melanin and protein. As such, it is easier to regard light-tissue interaction in terms of either water and/or organic molecules.

1.4.2 Scattering

Scattering is the other important variable for determining light propagation in tissue. The phenomenon arises from the different relative refractive indices of the various cellular substrates and molecules with respect to water, which is the main constituent of biological tissues. The scattered light undergoes further reflections and scattering, until it is either absorbed or escapes from the medium. In effect, the scattering process affects the shape and volume of the heated tissue from the light-tissue interaction. There are two main scattering mechanisms. Surface scattering results from rough and undulated surfaces. A rough surface is defined as one with valleys (troughs) which are slightly larger than the incident wavelength. Bulk scattering results from defects in the materials such as impurities and deformations.

1.4.3 Radiation Penetration Characteristics

The most important consideration in predicting laser-tissue interaction and the distribution of light within irradiated tissue is its overall attenuation (power loss) as light travels through the tissue, as shown in Figure 1.3. This is dependent on the ratio of absorption to scattering, which is a function of the incident wavelength and tissue type. Figures 1.4 shows the absorption and tissue penetration with the various light wavelengths. Laser light distribution in tissue is a complex problem mainly due to the structure and geometry of tissue and the variability of its optical properties.

Beer's Law gives an approximate estimation of light distribution in tissue [Carruth and MacKenzie,1986]. It describes the absorption of light in an isotropic medium. The extinction length is the distance light travels through the medium before it is absorbed to a point where 10% of the incident light remains. The remaining light is in turn attenuated by another factor of ten as it travels through the next extinction length, and so forth. Histology studies show that minimum depth of tissue damage in laser applications tends to be between one absorption length (depth when 63% of light is absorbed) and one extinction length.

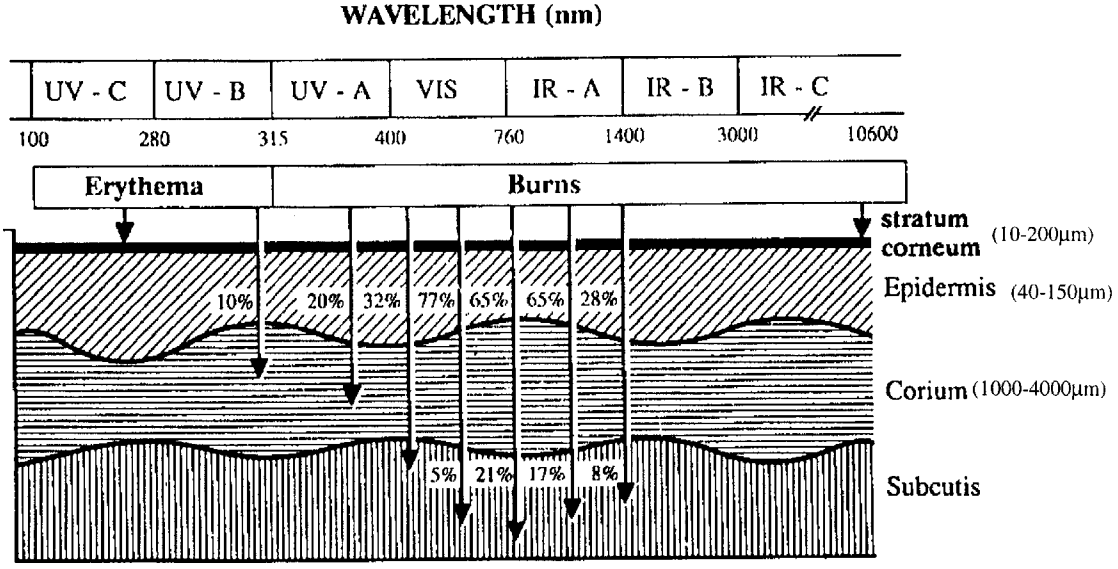

Figure 1.3 Spectral behavior of human skin, indicated is the residual intensity(Muller et al,1988)

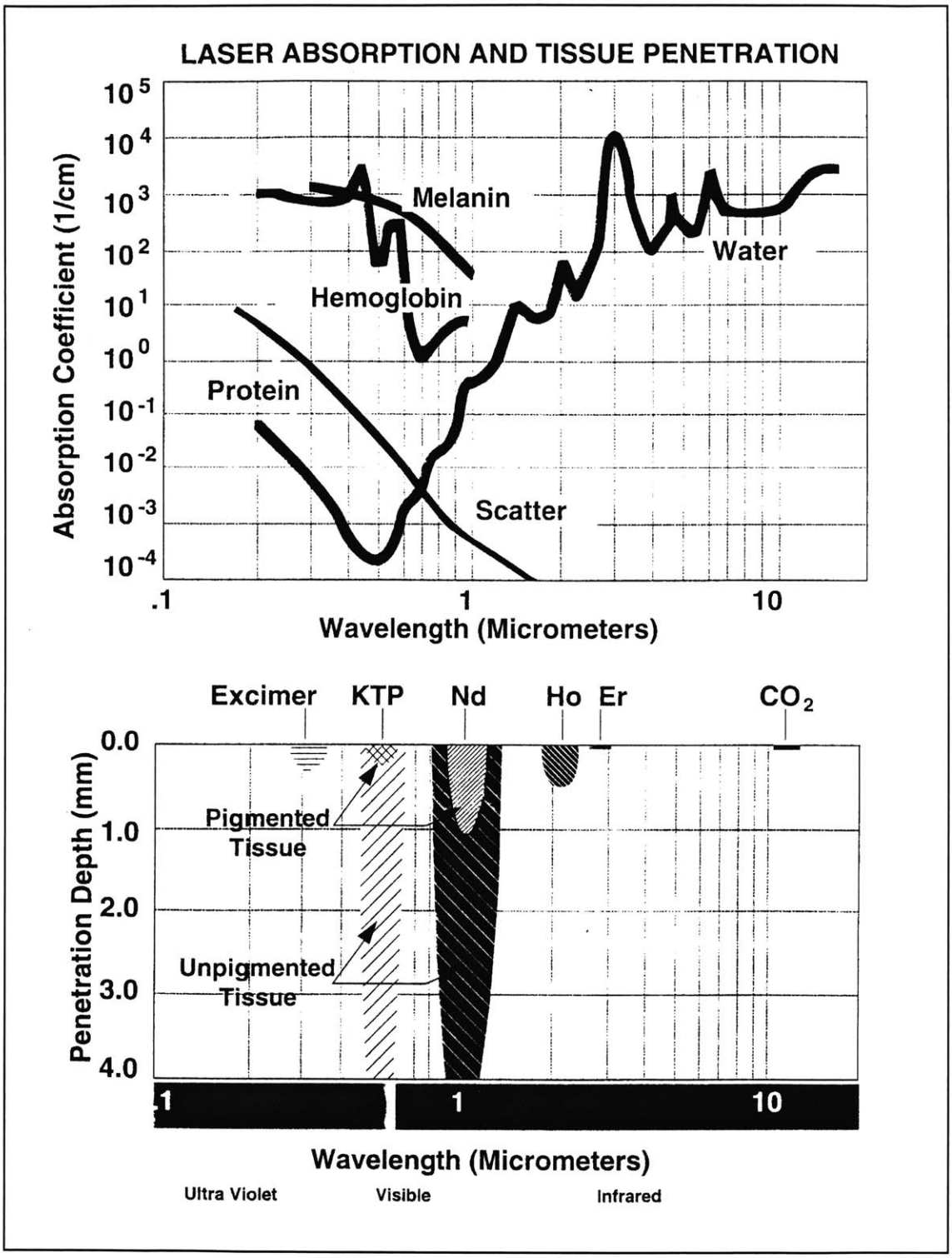

Figure 1.4 Laser absorption and tissue penetration (Coherent Inc.)

1.5 Laser – Tissue Interaction

The main energy transfer mechanisms in biological tissue have been described in the preceding chapter. Surgeons have tried, over the years, to utilize such interactions to advance the field of laser applications in medicine. For medical treatment, three major classes of interaction can be defined: 1) Photochemical interaction, 2) Thermal effects, and 3) Ionizing effects. The combined effect of the laser power density, energy density and interaction time will determine the interaction type, as illustrated in Figure 1.5.

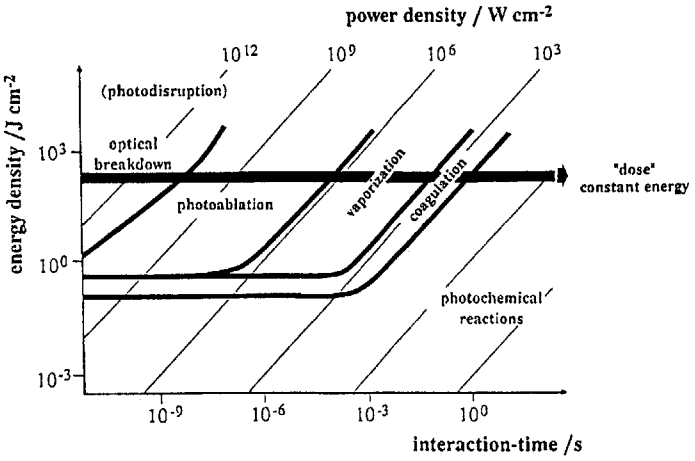

Figure 1.5 Energy density, power density and interaction laser time (Muller et al,1988)

1.5.1 Photochemistry

There are four main reactions of the photochemical mechanism: photoinduced isomerization in bilirubin degradation, photoinduced charge production in the visual process, photoinduced synthesis in plants and photoinduced dissociation in photodynamic therapy (PDT).

1.5.2 Thermal Effects

Thermal effects are due to light absorption, which causes a change in the tissue temperature. This forms the main process in laser applications.

a) Heat Conduction

Heat is produced when tissue absorbs light. The heat then travels through the tissue by conduction. This process is known as thermal relaxation (TRT). The time it takes the heat to penetrate a given distance is proportional to the square of the distance.

b) Coagulation (60°C –100°C)

The depth of tissue heating determines the coagulation effect. This is achieved by heating the tissue to approximately 80°C for a few seconds. The tissue retracts because of the desiccating effect but the overall structure is not destroyed. Coagulation is affected by the absorption length and thermal relaxation. This procedure is used for the removal of highly vascular tissue to prevent excessive bleeding. Coagulation is favored when working with small and delicate tissues in order to minimize thermal damage and preserve function. To achieve a particular coagulation depth, a long absorption length laser can be applied for a period long enough for absorption to heat the desired tissue. Alternatively, a short absorption length laser can be used and held in place long enough for heat conduction from the surface tissue to the desired depth to take effect.

c) Ablation (>300°C)

Ablation is achieved when an intense beam of laser rapidly heats the biological tissue above the boiling point of water. The water in the tissue vaporizes and carries the remaining constituents of the ablated tissue. The rate of ablation is highly dependent on the rate of deposition of laser energy into the tissue. When laser light is applied, adjacent

tissue is heated by absorption and the heat is then conducted to the surrounding tissues leading to coagulation. Heat that is not conducted would cause an intense rise in temperature and lead to tissue ablation. The biggest challenge faced by surgeons is in controlling the combined effect of ablation and coagulation. A complementary effect from ablation is the low degree of beam penetration into the tissue. This enables the surgeon to perform extremely delicate incisions or dissections of vessels or nerves.

d) Charring (100°C –300°C)

Charring is the carbonization of the tissue due to overheating. This occurs when the power density is less than critical ablation power. Charring results when the vapor plume that carries the heat away, does not occur fast enough, leaving a significant amount of heat in the tissue. The tissue then becomes dry and desiccated. This can be avoided using power densities higher than the critical value. However, most laser beams have a Gaussian distribution of power density across the beam diameter with maximum densities in the center. This results in tissue charring at the edges of a process that is being ablated cleanly in the center.

1.5.3 Non-Thermal or Ionizing Effects

Tissue ionization results from short and extremely high-energy pulses occurring within a narrow range of threshold intensities. The field strength is high enough to separate chemical bonds as well as the electron shells from positively charged nuclei of atoms, thus forming plasma. The formation of a shock wave results in mechanical shattering of the target. This could result in the fragmentation of the hard tissues or rupturing of membranes.

1.6 Lasers in surgery and medicine: Current applications

The use of lasers in medicine is growing with more than 1 million patients worldwide today. Lasers are even used to supplement conventional surgical tools such as scalpels. Figure1.6 shows the wavelength of popular lasers used in medical applications. Table 1.1 gives a basic overview of the applications of lasers and laser technology in medicinal and surgical practice.

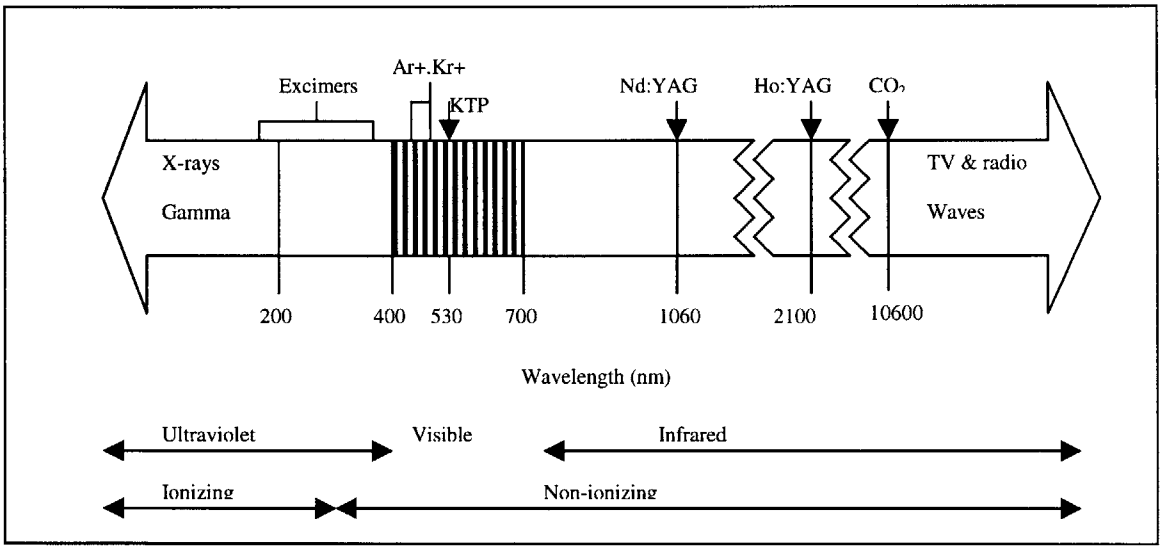

Figure 1.6 Wavelengths of popular lasers and the electromagnetic spectrum (Trost et al,1992)

Laser	Wavelength (nm)	Laser (type)	Tissue Effect	Discipline	Typical application
Excimer	193,249 308,351	Very short pulses	Ablation with little thermal damage	Ophthalmology Cardiology	Corneal surgery Laser angioplasty
Argon ion	488,514	Continuos	Coagulation	Dermatology	Port wine stains Tattoo excision
			Vaporization of lesions	Gastroenterology Gynecology Otolaryngology	Bleeding lesions Menorrhagia Bleeding lesions
		Pulsed		Ophthalmology	Retina reattachment Iridectomy Glaucoma
Dye	400-1000	Continuos	Sensitizer triggering	Oncology (+others)	Photodynamic therapy
		Pulsed	Selective absorption	Dermatology	Port wine stains
			Plasma	Urology	Laser lithotripsy
Neodymim –yttrium-aluminum-garnet (Nd:YAG)	1060	Continuos	Volume heating	Gastroenterology General	Homeostasis Tumor cure Cholecystectomy
		Pulsed	Plasma and shock	Urology Ophthalmology	Laser lithotripsy Tumor destruction
CO2	10600	Continuos, long pulses	Precise cutting	Surgery	Tissue removal Laser surgery

Table 1.1. Medical lasers and their applications (Abraham Katzir, 1993)

1.7 Laser dermatology

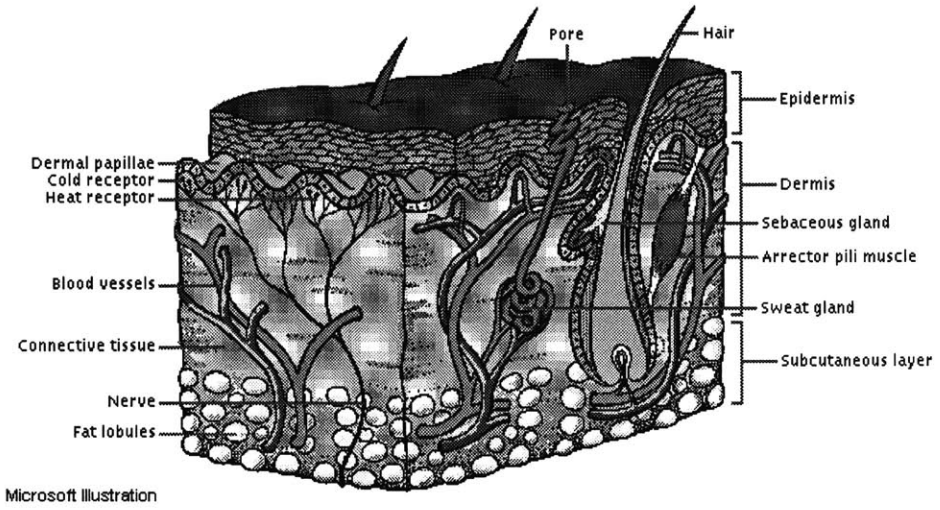

Figure1.7 Cross section of human skin (Microsoft Encarta 1998)

Skin is a complex, highly dynamic, variable and multi-layered optical medium. Chromophores tend to be confined to discrete layers while scattering agents tend to be distributed uniformly throughout this turbid media. Human skin responds differently to the energy density (fluence) and wavelength of the impinging laser. As the fluence is increased, the effects change from biostimulative to inhibitory and then to cytotoxic. At higher energy levels, thermal effects dominate with tissue shrinkage followed by cell necrosis and then tissue ablation. Types of lesions to be treated dictates the wavelength used. New applications of lasers are constantly being discovered with recent promising breakthroughs in microvascular welding of blood vessels and peripheral nerves. Outlined below are some of the more common laser dermatology applications.

1.7.1 Vascular Lesions and Port Wine Stains

Vascular lesions respond well to visible wavelengths and superficial non-pigmented skin lesions respond to wavelengths that are well absorbed by water. Examples of vascular lesions are port wine stains, cavernous angiomas, Kaposi's sarcoma and malignant vascular tumors. Port wine stains have a characteristic pink, red or purple color because of abnormalities in the capillaries in the outer dermis. The color is result of the blood in these capillaries showing through the clear epidermis. Argon laser has been shown to have a favorable response in treatments. The blue-green light is readily absorbed by the oxyhaemogloblin and passes through the transparent epidermis with minimal absorption. This results in thermal damage and thrombosis of the abnormal capillaries. This treatment would not work for highly pigmented skin. Tunable dye lasers have also been tried for port wine stain treatment with promising results. Argon laser is also used to treat the leashes of fine superficial leg veins associated with varicose veins.

1.7.2 Skin Lesions

CO_2 is used to excise a wide range of skin lesions and ablate recalcitrant warts. There is some potential advantage in treatment of malignant tumor because the laser seals the lymphatic channels , reducing the tumor spread. Incisions made with CO_2 laser lead to coagulation of small blood vessels and localized heat necrosis, resulting in longer healing times compared to regular scalpels.

1.7.3 Tattoo removal

Ruby laser is used occasionally for treatment of pigmented lesions and removal of blue and black tattoo. Previous treatment (CO_2 and Argon) modalities destroyed the tissue

that contained the tattoo pigment. This method caused unpredictable scarring. Current Q-switched ruby lasers bombard the pigments within the tattoo. This causes the pigments to absorb the high densities of energy and fragment. As a result, there is minimal scarring or epidermal damage, leaving a good cosmetic finish.

1.7.4 Plastic surgery

CO_2 and Nd:YAG have remained the most popular laser systems with dermatologist and plastic surgeons, although more recent systems have used xenon-fluoride excimer and heavy metal vapor lasers. Skin resurfacing methods include treatment for facial rhytides, acne scars and aging skin('face lift'). Highly controlled ablation processes can be used for skin resurfacing and rejuvenation. This is achieved by rapid removal of subsequent layers of tissue with minimal charring and thermal damage. The resultant phagocytosis produces a good cosmetic finish.

1.7.5 Hair Removal

Heredity, endocrine disease and drug therapy are some of the causes of excess hair growth in unwanted areas of the human body. The hair follicle represents a well defined physical target, which has an approximate depth of 4mm and a mean diameter of 100μm. Permanent changes in the follicle can occur as a result of laser energy interaction. Depending on the procedure, this could lead to changing of hair color, growth retardation and elimination of hair.

1.8 Laser hair Removal

The use of lasers in hair removal represents a new challenge for laser technology in dermatological uses. Laser hair removal relies on the destruction of hair follicles based on the theory of selective photothermolysis. The interaction between laser energy and hair follicles has been known for almost 30 years now, but the approval of the first laser (Thermolase®) for these applications by the Food and Drug administration (FDA) came only in early 1995. Hair revolves through three phases of growth: anagen (growth phase), telogen (resting) and catagen (regression). It is desirable for the laser to penetrate to the depth of the hair follicle during the anagen phase. The depth of the hair follicle, the anagen period, and the minimum number of treatments required vary between patients and even differ over the various body areas.

The current potential market size for laser hair removal is approximately $1–$2.5 billion in the United States. [Moretti et al, 1996]. The use of light and laser hair removal is emerging with four main classes of devices: the Nd:YAG lasers with a carbon cream agent, the ruby lasers, the alexandrite lasers, and the polychromatic broad band light source of flashlamp technology. Table 2 provides pertinent information about the products currently available and under development for light-based hair removal.

Product	Wavelength	Specification	Comment
Thermolase SoftLight®	1064nm Nd:YAG	12-18nsec, 3.0 J/cm^2, 7mm spot, 1,2 5,10Hz	Wax out hair, use carbon cream, and lase off carbon. Hair color is not a factor for treatment, recommended for Fitzpatrick skin types I to III. SoftLight© is being developed without the waxing step.
Palomar E2000®	694 nm ruby	3msec, 10 to 50J/cm^2, 7 to 10 mm spot, 1 Hz	Treats Fitzpatrick skin types I to IV. Cold room temperatures to keep laser below 85° F. Contact cooling in hand piece. Works best on dark hair and light skin.
Sharplan EpiTouch®	694nm ruby	Q-switched: 25 to 40nsec, 10J/cm^2, 3 to 5 mm spot. Free run: 1.2msec, 40J/cm^2, 5 to 6 mm spot, 1.2 Hz	Uses cooling gel. Redness is present 3 to 4 days. 40% to 80% regrowth > 12 weeks, 30 % regrowth after two weeks treatment. Works best on dark hair and light skin.
Mehl Biophile Chromos 694®	694nm ruby	500µsec, 10 to 15 J/cm^2, 7mm spot, <1.0 Hz	Mark 1®, 20% regrowth 190 days after two treatments. Mark II®, will have a pattern generator and diagnostic light beam. Works best on dark hair and light skin
Sharplan Epitouch® Alex	755nm alexandrite	2msec, 5pps to 10 J/cm^2	FDA approved. Now released in the USA. Scanner is anticipated in the first quarter of 1998
Candela GENTLELASE®	755nm alexandrite	2 msec pulse	Being developed in the USA as an answer to Long Pulse Infra-Red (LPIR)
Cynosure LPIR®	755nm alexandrite	20 msec pulse, 1pps, to 20 J/cm^2	Clinically proven device reduces trauma and hypopigmentation to epidermis.
Energy Systems Corporation (ESC) EpiLight®	590 to 1200nm flashlamp	Variable msec, J/cm^2, 8x 35mm spot, 2 to 5 multipulse	Broad band energy. Company claims to have data for Fitzpatrick skin type V and above, and for treatment of gray and blond hair.

Table 2 Hair removal devices and their basic specifications. (Clark, 1998)

The potential market for hair removal appears larger than for any other laser application at this time. As the market, devices, and methods mature, a larger spectrum and segment of the patient population can be treated with laser hair ablation. Skin anatomy and tissue optics is such that it is difficult to achieve the light levels needed for selective photothermolysis of the deep portions of the hair follicle. A complete understanding of light/tissue interaction and how wavelength, time and energy come into

play, will enable manufacturers of laser hair removal devices to create a superior product. Speed of removal and reduced discomfort to the patient are the other factors that would determine the success of the laser product.

The MIT/MI scanner was developed to address the speed and comfort issues of the laser removal procedure. The scanner was designed to be used in high-volume medical practices, as well as the growing spa and salon markets, since both providers and consumers will benefit from dramatically improved speed, ease of use and consistency. The scanner was developed as a complimentary device to the Palomar E2000® system.

1.8.1 Palomar E2000™ Ruby Laser System

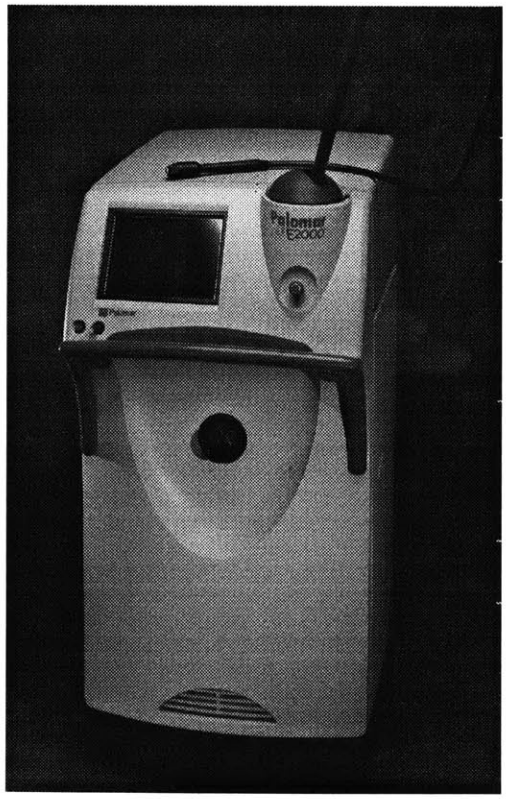

Figure 1.8 Palomar E2000™

The Palomar system is based on the work of Rox Anderson after years of research at the Massachusetts General Hospital Wellman Laboratories of Photomedicine, one of the world's leading medical research institutions. FDA approval for this system was received in July 1996. The 694nm-wavelength ruby laser light targets the melanin in the human tissue. The wavelength falls in the light spectrum that affords a desired combination of absorption by melanin and deep penetration into the dermis. Melanin in the hair shaft, follicle and epidermis provides a chromophore for light absorption. The system is most suitable on patients with dark hair and light skin tone because of the competition of light absorption between hair and skin melanin. The epidermis contains eumelanin (responsible for brown/black coloration) through which the light must pass to reach the follicle. The goal of this method is to maximize follicle damage with minimum epidermal damage as shown in Figure1.9. It is not recommended for Fitzpatrick IV skin types and above and for light hair tones.

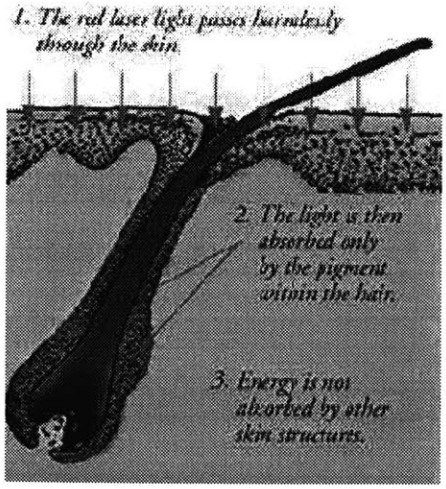

Figure 1.9 Selective photothermolysis of hair follicle (Palomar Medical,Inc)

The energy is delivered by a 10mm EpiWand® (Figure1.10) hand piece through a thermally cooled tip. Most laser light is generated using either sub-micro-second pulses (Q-switched) or longer pulses. The E2000™ system uses a normal long-pulse to broaden the zone of thermal damage within and around the follicle. In general, longer localized laser pulses heat a larger volume and require greater fluence to achieve selective follicular damage. 10 J/cm ^{2} (darkly pigmented individuals) to 50 J/cm ^{2} (fair-skinned) is the fluence range of the E2000™ system.

The 3 msec pulse duration falls within the 'ideal' Thermal Relaxation Time (TRT) of the hair follicle (0.8 to 3.1 msec [Clark,1998]) and on the lower threshold of the TRT of the epidermis (3 to 10 msecs [Grossman et al, 1996]). In addition to the standard 3msec pulse, the TwinPulse™ Mode system also has a unique pulse mode where two distinct pulses are emitted at 100 msecs. The pulse mode system coupled with the patented "Super Cooling" contact cooling hand piece (0 to -10 °C) delivers optimum energy to the reticular dermis while minimizing thermal injury to the epidermis. At this setting, it is possible to extract heat during the laser pulse while thermal confinement is maintained in the hair follicle. Heat is also conducted from the skin surface before and after each laser pulse by the cooling contact tip.

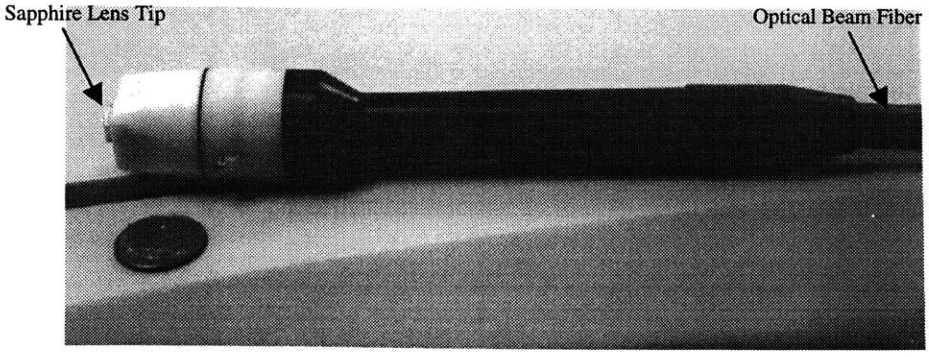

Figure 1.10 Palomar Medical EpiWand®

A high refractive index sapphire prism/lens is used to provide a convergent beam (approximately 20mm in focal length) at the skin surface and to increase beam coupling into the skin as compared with air as the external medium. Convergent beams increase irradiance at a given depth compared to collimated beams. The system also has a relatively large hexagonal spot diameter of 10mm to optimize light delivery. The E2000^{TM} system relies on a forceful compression of the skin to temporarily reduce blood flow and to compress the dermis significantly in order to reduce the distance between the surface and hair follicle. The system utilizes "Contact Sensing" technology, in which the laser energy is triggered by sensing optimal epidermal temperature, assisting the provider to achieve the most desirable long-term effect, while also maximizing laser safety. From experimental observations, the optimal temperature is usually achieved when the cooling hand piece is firmly held against the skin surface at a force of a few pounds. Figure1.11 illustrates the compression of the sapphire lens tip of the EpiWand® on a cross section of the epidermis.

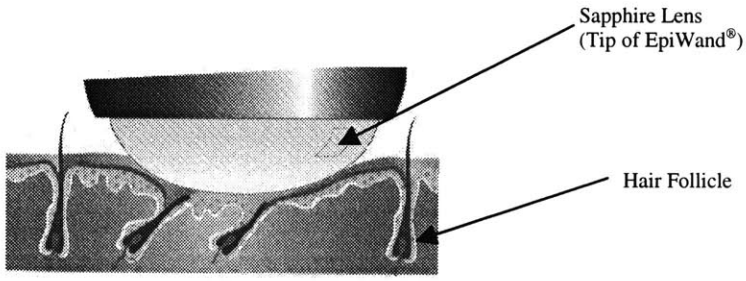

Figure 1.11 Close-up illustration of sapphire lens pressing on skin cross section (Pal- Medical,Inc)

The treatment technique consists of preoperative shaving of the treatment site to prevent long and pigmented hairs that may lie on the skin surface from conducting light energy to the adjacent dermis. Treatment is performed by delivering light in a pattern of

laser pulses, adjacent to one another, while the contact cooling piece is firmly held against the skin before each pulse. The E2000™ system's unparalleled potential speed is particularly important in the treatment of large areas such as the back and legs. The system is, in theory, capable of treating a pair of female legs in four hours, or a man's back in about half that time. It could allow the surgeon to dramatically increase patient flow, which potentially lowers the cost per treatment. The problem is that the provider cannot manipulate the hand piece quickly enough to capitalize on the laser's inherent speed, while trying to maintain positional and application force accuracy.

To match the maximum pulse rate of the E2000™, the scanner must be capable of operating at a 1 Hz hit rate. In other words, it must move from one location to the next in less than one second . Figure 1.12 shows the EpiWand® with an illustrated contact grid that simulates the contact zones on the skin. When located above the correct grid position, the scanner will move the wand down in the Z-direction. When the force sensor detects a proper applied force, the scanner will hold position until the laser is fired. Immediately after contact firing, the scanner would retract the wand fully in the Z-axis before moving along the X-direction to the adjacent grid position. This would prevent the wand from dragging on the patient's skin. The scanner would raster the hand-piece along the X and Y directions, moving up and down the Z direction at each step, until the whole grid is completely treated. Each firing cycle should take place no longer than one second. In most cases, the laser hand-piece has to hold position for approximately 500 msecs before achieving optimum firing temperature. This leaves the scanner less than half a second to locate the next grid position.

The development and design of the automated precision scanner will be described in chapter two of this dissertation. Chapter three will cover the system modeling and control strategy of the scanner. Upon completion of the scanner, a series of tests were conducted to gauge its mechanical operating performance. The details of the experiments and a brief discussion of its performance are given in chapter four. Tests indicated that a velocity sensor that would provide actual velocity of the device relative to the skin, has to be developed. Chapter five describes the development of a series of velocity sensors suitable for this application. The dissertation is concluded in chapter six, which describes the clinical performance of the interfaced laser-scanner system on a patient . The final chapter also provides a discussion on the scanner and velocity system performance.

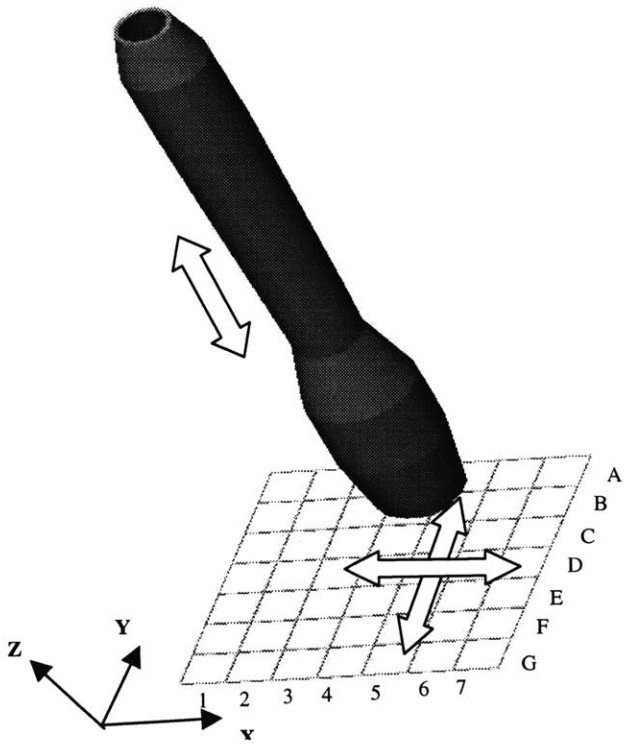

Figure 1.12 EpiWand® contact grid on skin surface

2 Development and Design of an Automated Precision Scanner

2.1 Functional Requirements and Constraints

There were a number of functional requirements that had to be met in the mechanical design of the scanner. These requirements shaped the final form of the machine. Potential cost of production was another major factor in the design process. The prototype machine had mass production potential so it was desired to keep cost down. As the prototype was one of a 'proof-of –concept' machine, more functional requirements were included to add versatility and help identify critical variables. Some of the functional requirements are listed below:

1) The scanner had to be fully automated.
2) Variable scanning patterns.
3) Scan range:

   X&Y-direction: minimum 2 inches

   Z-direction: minimum ¾ inches
4) Repeatability:

   X&Y-direction: 0.01 inches (250 microns)

   Z-direction: 0.004 inches (100 microns)
5) Cycle time:

   Z-direction: ½ inch in 0.05 seconds

   X&Y-direction: 1/5 inches in 0.1 seconds
6) Force sensing range of 5 lbs.
7) Communication between laser system and scanner.

The first requirement stipulated that there should be minimal human interference. This necessitated the use of a computer control system to automate and coordinate the electrical-mechanical structure.

The second requirement is driven by the need to have a flexible machine that can be used on various parts of the human body. The main applications would include the thighs, back and arms. The human arm has a relatively high curvature and aspect ratio. To accommodate this narrow area, the machine has to have a minimum scan area.

The third requirement is repeatability, and not accuracy of the X-Y direction. As most laser beams have a Gaussian distribution of energy density across its diameter, some overlaps in firing zones are recommended. This has the tendency to distribute the energy density more evenly across a scanned profile. The level of overlapping should be very repeatable to ensure consistency in treatment.

The fourth requirement satisfies one of the main motivations of an automated system, which is to increase throughput. Given that the scanner has approximately 400 msecs to position the laser hand-piece between successive firing for a 1 Hz repetition rate, the axes must be capable of high speeds. The total accumulated time from the design specification is 300msecs. This allocates ample time for the system to achieve steady state in all three axes before initiating fire. The requirement gives minimum speeds of 2 inch/sec for the X and Y stages and 10 inch/sec for the Z-stage. These velocity values are calculated using a rectangular velocity versus time profile. However, almost all systems are driven by trapezoidal profiles and this would require a higher maximum velocity to maintain the same distance and time specifications.

The fifth requirement is important for the laser system to initiate. Optimal firing conditions are achieved when a proper force is exerted by the contact cooling hand-piece on the skin.

Finally, some form of communication between the laser system and scanner would increase the performance with both systems coordinating their operations. Pulses of 3 msecs trigger the E2000^{TM} system. A quick sensing trigger mechanism on the scanner had to be designed to accommodate the high pulse rates of the laser.

2.2 Design Issues

2.2.1 General Concepts

During the initial stage of scanner development, many concepts were created to address the functional requirements. The first concept (Figure 2.1) was a relatively large structure with 3 ½ feet by 1-foot footprint. The main motivation behind this design was to fully automate the laser process over the length of a patient's leg and thigh with minimal operator interference. For good clinical results, it is desired to bring the laser hand-piece perpendicularly to the skin surface. The system shown in Figure 2.1 has a curved axis to accommodate the curvature on the human body. However, a market study conducted by the sponsoring company concluded that as a first step towards automation, providers preferred a hand-held machine to a large fully automated system.

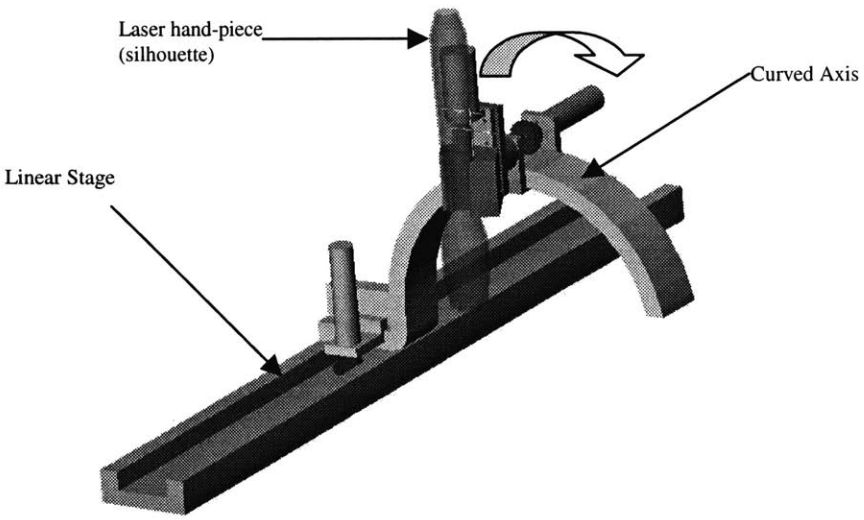

Figure 2.1Full length automated system concept

The second concept was a machine with an overall footprint of 5 inches by 5 inches. This concept was significantly smaller and could be handled by an operator. This necessitated a light and compact design. The operator would bring the machine to the patient's body and hold it in place until the end of operation. The added advantages of such a system would be its low production cost and safety aspects. A small scan area has a relatively flat curvature making it possible to move away from the curved axis design. Figure 2.2 shows the design approach that was taken. The machine has two support handles for the operator. All three axes are packaged within the 150 cubic inches central volume.

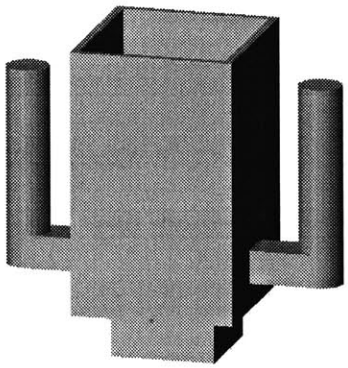

Figure 2.2Handheld scanner concept

Further refinements of the second concept lead to a leaner design as shown in Figure 2.3. Different legs were designed for the final concept because of the need to have a proper mount on the skin surface. This design works especially well on highly curved surfaces. The mount has a four point contact configuration, a slight modification to the regular three point contact on kinematics joints. The fourth leg was added to increase

mounting orientation stability. The height of central casing was also reduced to cut down on weight. This further reduced the working volume available. The three axes are placed in a stacked configuration. Starting with the Y-stage at the bottom followed by the X-stage and the Z-stage at the top.

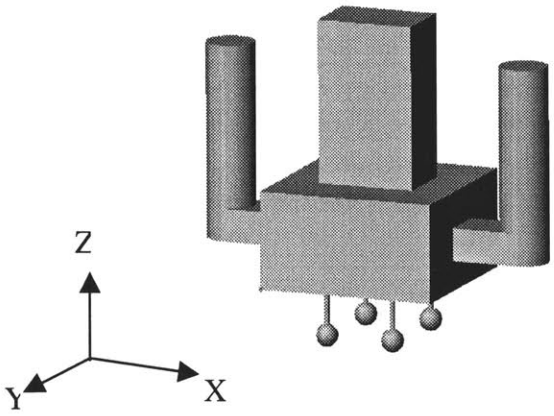

Figure 2.3Final design of casing

2.2.2 Linear Stage Selection

The basic design of the three stages is quite straightforward. There is a wide selection of linear stages on the market based on different methods of actuation.

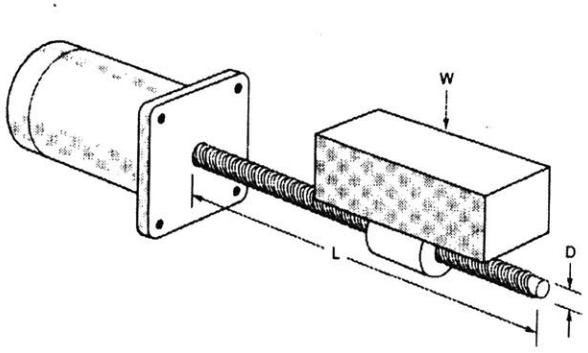

Figure 2.1 Ballscrew driven actuator

The first and most conventional design of linear stage uses a ballscrew as the means of actuation. An illustration of such a ballscrew mechanism is given in Figure 2.1. The ball screw system is relatively simple and has good accuracy and repeatability. The limitation in its use is the 'critical speed' of the system. The critical speed occurs when the screw is turning at speeds nears its natural bending frequency. The system can then become resonant and the failure may follow.

The equation characterizing the critical speed for a given screw, as given in the Ballscrew and Actuators C0.(BSA),Catalog, is:

$$C_s = F \; x \, 4.76 \; x \, 10^6 \, x \, \frac{d}{L^2}$$

C_s = *Critical speed*

D = *Root diameter of screw*

L = Length between supports

F = End support factor (1.47 for one end fixed)

Based on a ballscrew length of 4.5 inches, the critical speed will be around 130,000 rpm. (using a lead screw of 3/8-inch diameter screw). With a normal ball screw pitch of 0.15 inch per turn, the maximum speed of the carriage would therefore be limited to 250 inch/sec. This certainly meets our requirements. Ballscrew assemblies are very streamlined because of their inline drive set-up. This suits applications where a high design aspect ratio is required, as in the case of the Z-axis.

The second option is the belt drive linear stage. A generic belt driven stage is shown in Figure 2.2. Belt drives have low stiffness due to the belt compliance and are only able to transmit low linear forces. This makes it undesirable as the choice of actuation for the Z-stage. However, the belt system is also cheaper and lighter.

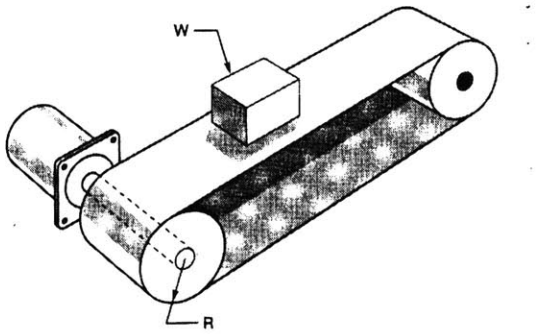

Figure 2.2 Belt driven actuator

The final option considered is the rack and pinion drive (Figure 2.3). Its main feature as far as machines are concerned is that racks can be placed end to end to increase range. The drive's biggest drawbacks are that they generally exhibit backlash and do not provide a mechanical advantage the way a ballscrew system does. It is also difficult to

obtain the optimal transmission ratio and a speed reducer is often used with the motor that drives the pinion. This drive is usually used in systems that require long travel distance. The advantage of the rack and pinion system over the belt drive is that they can be made more compact. Due to the space constraints in our system and the simplicity in design, the X and Y stages were based on the rack and pinion drive.

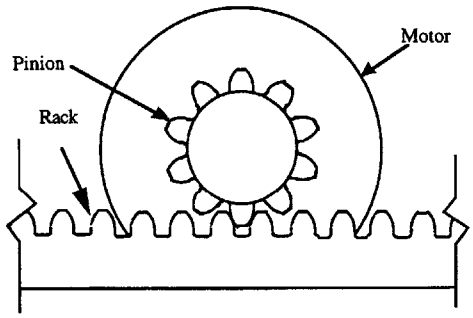

Figure 2.3Rack and pinion driven actuator

Other actuator alternatives such as friction drives and linear electric motors were not considered because of some drawbacks in application. Friction drives have low drive force capability and moderate stiffness and damping. Furthermore, they have minimal transmission gain and are very sensitive to the drive bar and capstan cleanliness.This makes maintainance an issue. However, friction drives have minimal backlash. The main disadvantage of linear motors is their high cost. They also develop less linear force than screw driven actuators and the inherent low damping complicates their control.

2.3 Design Concepts and Selection

After the drive systems were selected, the actuation of the stages needed to be determined. The application requires high-speed operation and moderate load capability. This necessitated the use of high power to size ratio actuators. Miniature DC brushed servomotors with integrated encoders and gearheads were chosen for all three axes. The control loop was closed using simple PID control based on the encoder feedback.

2.3.1 Z-Stage Design Alternatives and Concept Selection

Many concepts were generated for the Z-stage design during the initial stages of brainstorming. One of the major concerns in designing the Z-stage was its compactness. The entire assembly had to be packaged within a four inch cross sectional area and six inch height volume. The basic components of the assembly consisted of the force sensor, actuator, linear bearing, ballscrew and laser hand piece.

The force sensor required a minimum resolution of 0.05 lbs.-force and a range of up to five-pound force. Load cells were not considered because of their high cost. The positioning strategy for the Z- direction motions is relatively straightforward. Brushed servomotor was chosen for the Z-stage. The motor came equipped with a magnetic encoder of 16 PPR before quadrature. When connected to a ballscrew of 0.15 lead, this satisfied the 0.01 inches resolution stipulated in the functional requirements. Three concepts for force measurement were initially considered.

The first concept uses strain gauges to measure the applied force. Figure 2.7 shows a motor driving a ballscrew that is connected to the laser mount carriage through a cantilever arm. The laser mount carriage is constrained to move axially with a linear

bearing. A silhouette of the laser head is added to show its relative position in the whole assembly. The cantilever arm serves as a strain amplifier member for the strain gauges assembled in a Whetstone configuration. The assembly has few components and a simple design. However, preliminary calculations gave limited strain values in the cantilever member arm. Given the limited workspace, the length of the arm was restricted, resulting in lower strain values. This reduced the resolution of its force sensing capabilities.

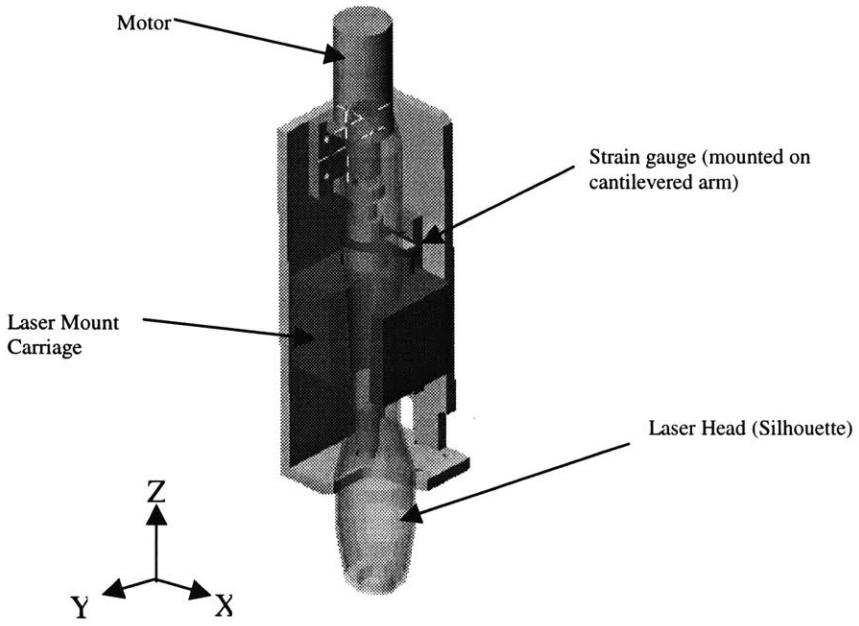

Figure 2.7 Strain gauge force detection configuration

The second concept utilizes a cam mechanism to regulate the compression force exerted by a spring of known stiffness. The motor turns a shaft that is connected to a cam mechanism. The cam in turn drives a roller that is part of the laser mount carriage. The concept is illustrated in figure 2.8. The cam angle limits the travel of the laser mount carriage. The design is relatively more complicated and the force applied is implicitly controlled by the cam angle.

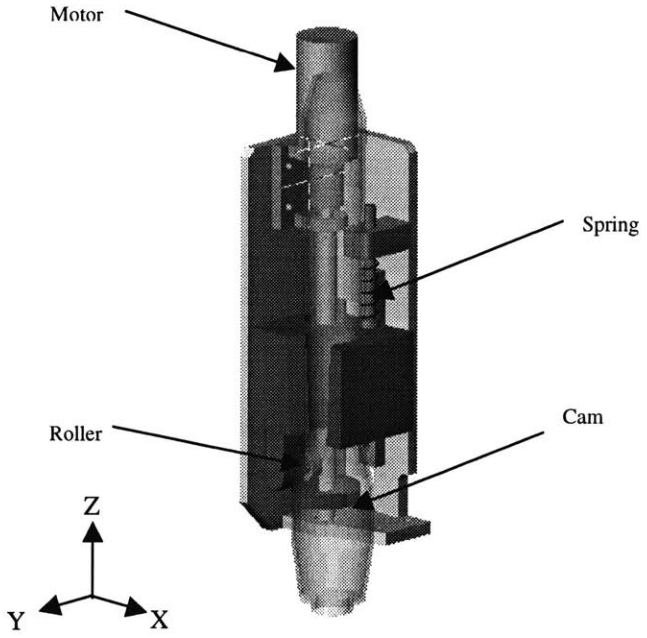

Figure 2.8 Cam driven force actuator

The third concept had a linear variable displacement transformer (LVDT) measuring the displacement of a compression spring of known stiffness as the means of measuring force. In figure 2.9, the motor drives a ballscrew that is coupled to a connector, which in turn drives the laser mount carriage via a compression spring. The motion of the laser mount carriage is guided by a linear stage. As the laser head makes contact with the skin, the axial force generated by the motor will create the spring compression force. The LVDT is capable of high-resolution measurement and replacing springs of different stiffness could vary the force range. This gives the system a high degree of versatility and was the design strategy that was chosen for the Z-stage.

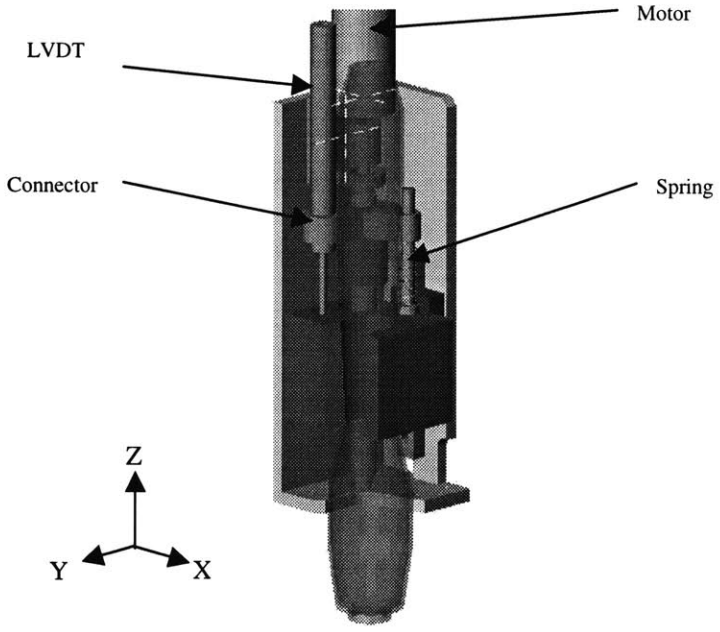

Figure 2.9 LVDT force detection configuration

2.3.2 Y-Stage Final Design

The scanner axes are stacked with the Y-axes on the bottom. The Y-axis has a high aspect ratio of 2:1 to keep the design compact. As such two linear bearings are required to provide a smooth linear motion , as shown in Figure 2.10.

The stage is driven through a 43:1 gearhead between the motor and the pinion drive to provide proper load matching. The use of gears with small motors allows high torque applications while maintaining a low weight. A DC Brushed servomotor with attached encoder with 16PPR before quadrature was chosen for the Y- stage. The achieved resolution was well within the functional requirements on the Y stage.

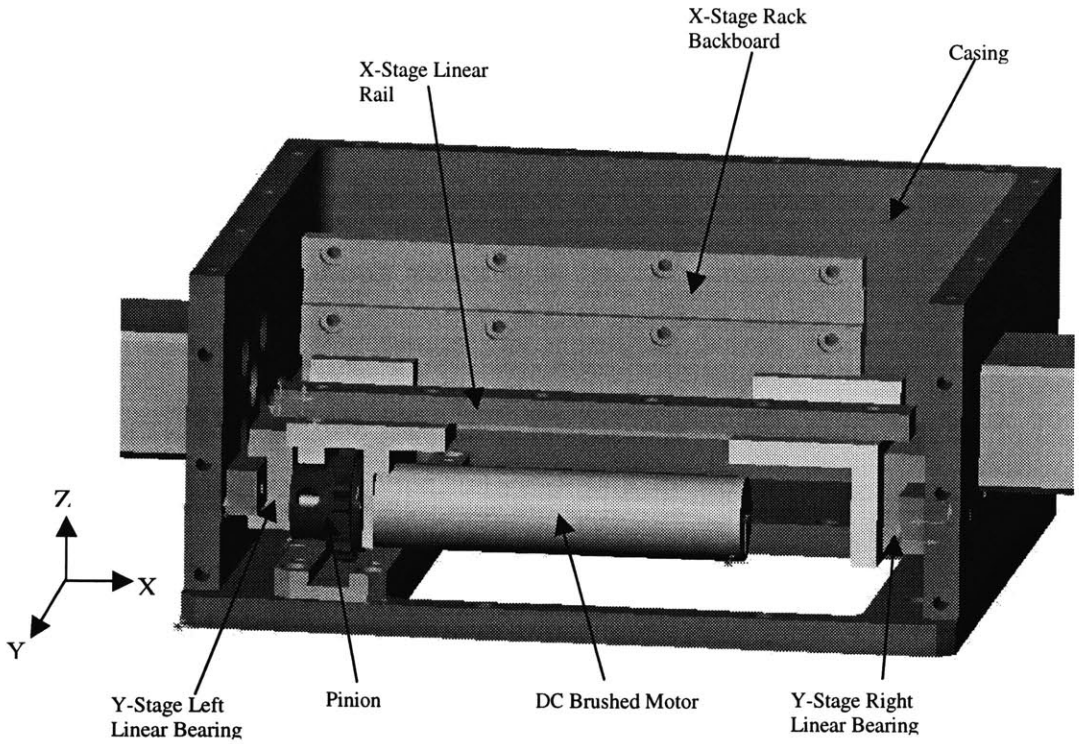

Figure 2.10 Final Y-stage design

2.3.3 X-Stage Design

To obtain maximum power efficiency, the motor armature inertia and the load inertia reflected onto the motor were matched. Gear reduction of 43:1 came closest to optimizing this ratio. Similar to the Y-stage, a DC Brushed servomotor with attached encoder with 16PPR before quadrature was selected. Resolutions of 0.0002 inches could be easily achieved especially with the gearheads attached. This was well within the functional requirements of the X- stage. The final X-stage design is shown in figure 2.11.

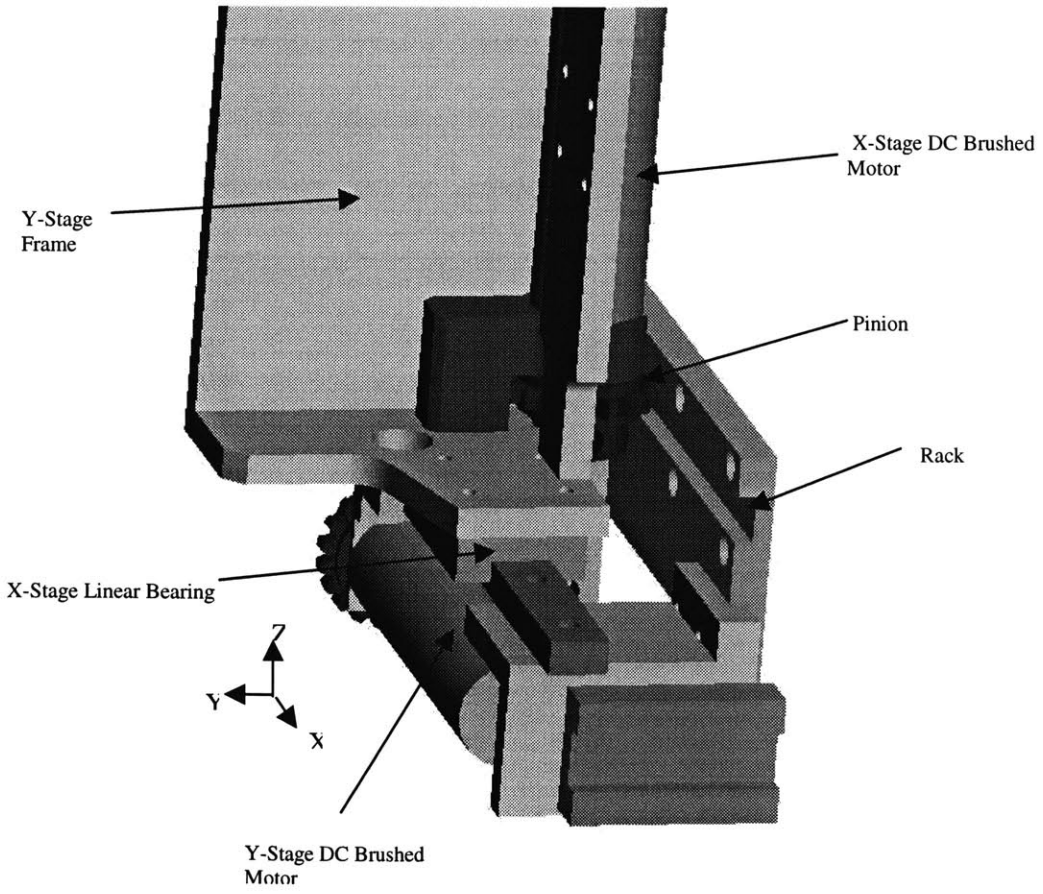

Figure 2.11 Final X-stage design

3 System Modeling and Control

A Digital Signal Processing (DSP) board drives all three axes, freeing up the host CPU for other task. A four axes PC-Bus Servo Motion Controller by Technology 80® was chosen. PID position control strategies were used on all three axes. A trapezoidal acceleration profile was chosen over the S-curve profile. Trapezoidal profiles are faster of the two styles when moving an equivalent distance. This makes it preferable for quick moving action. S-curves generate softer acceleration and deceleration, thus lowering inertia torques.

3.1 System modeling

The three axes are placed in a stacked configuration with the Z-axis on the top and X-axis on the bottom. To simplify the analysis of the system dynamics of the scanner, it is assumed that the performance of the X and Y stages are identical.

3.1.1 X & Y Stages

Both stages were designed to carry a structural load of 5 lbs. (~2.5Kg) through a rack and pinion actuator. Aluminum pinions of pitch diameter 0.8324 inches were used and connected to the motor via 43:1 gearheads. The calculated total polar moment of inertia reflected at the motor is approximately 0.02 oz-in^2 and is given by:

$$J_t = J_m + \left(\frac{Z_a}{Z_b}\right)^2 \left(J_{pin} + MR^2\right)$$

J_t = *Total polar moment of inertia*

J_m = *Inertia of motor*

J_p = *Inertia of pinion*

M = *Mass of structure*

R = *Radius of pinion*

$$\left(\frac{Z_a}{Z_b}\right) = \textit{Gear reduction ratio} \quad ; \quad J = \left(\frac{\pi \rho w (d)^4}{32}\right)(kgm^2)$$

3.1.2 Z-Stage

The stage is driven by a stainless steel ballscrew of dimensions given in section 2.1 of this chapter. The mass of the entire Z- stage assembly is approximately 3 lbs. 0.09 oz-in^2 is the inertia of the assembly that is reflected onto the motor. The equation is given by:

$$J_t = J_m + J_{screw} + M\left(\frac{p}{2\pi}\right)^2$$

J_t = *Total polar moment of inertia*

J_m = *Inertia of motor*

J_{screw} = *Inertia of the ballscrew*

M = *Mass to be driven*

p = *pitch of screw*

3.1.3 DC-Motor schematics

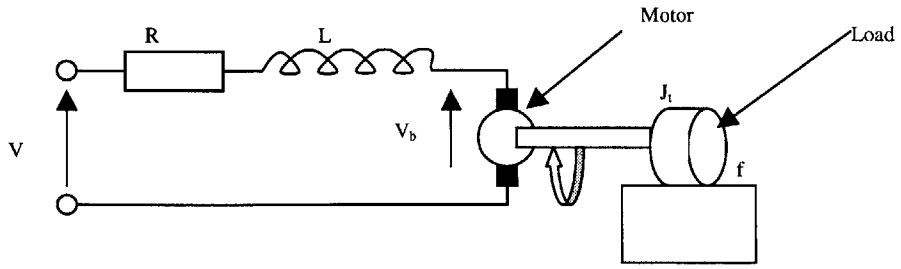

Figure 3.1DC-motor schematic

R = Armature resistance

L = Motor inductance

V = Voltage source

V_b *= Back emf*

J_t *= Total inertia torque of plant reflected on motor*

f =Friction

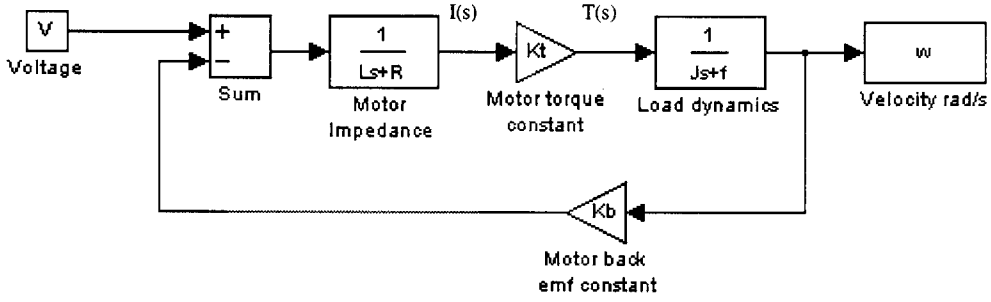

Figure 3.2DC Motor and load dynamics block diagram

3.2 System control

DC servomotor positioning systems generally act as low pass filters and filter out all frequencies above the bandwidth frequencies. The servo bandwidth will determine the limits of the systems performance and its dynamic range. The servo motion controller has a 16 bit Digital-To-Analog (DAC) command and outputs +/- 10 VDC. Three linear servo amplifiers with gains of 2.4 were each used to drive the individual motors. This facilitated the use of motors with low inductance and negligible electrical time constant {(L/R)~0}. The frictional forces were also neglected because of the relatively low coefficient of friction in the miniature linear bearings used in all three stages. Figure 3.3 illustrates the basic PID controller strategy used on all axes.

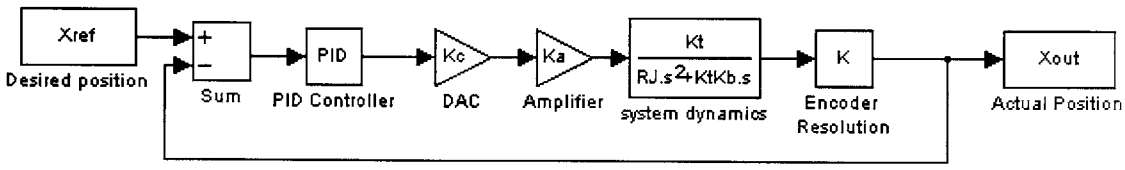

Figure 3.3 Block diagram of PID servo controller scheme

The third and fourth functional requirement stipulated that the scanner must be capable of rapid motion in all three axes with sufficient resolutions:

- Z-direction: 1/2 inches in 0.05 seconds with resolutions of 0.01 inches
- X&Y-direction: 1/5 inches in 0.1 seconds with resolutions of 0.01inches

To achieve such performance specifications, proper gain values for the PID controller had to be obtained. The analysis can be simplified by working with a step response. For the all three axes, the maximum allowable design overshoot is 5%.

Given the rise time and maximum overshoot allowed in the system, the proportional and derivative gain could be approximated using a PD controlled system. Once the Kp and Kd values have been obtained, the system response of a full PID will be analyzed to provide an optimum Ki value.

Determining the Kp and Kd-using a PD controller approximation

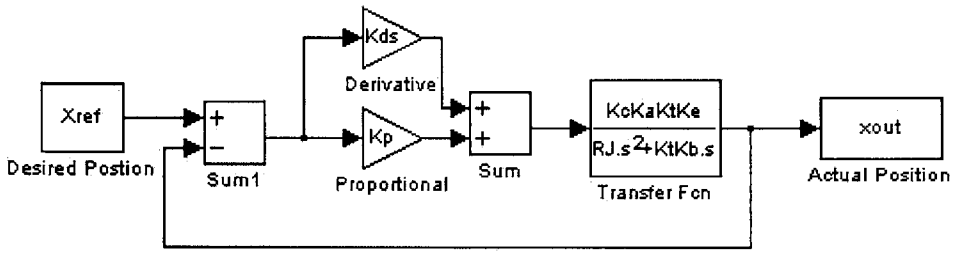

Figure 3.4 Block diagram of PD servo controller

The closed loop transfer function is:

$$CL = \frac{\frac{K}{\tau}\left(K_p + K_d s\right)}{s^2 + \frac{(1+KK_d)}{\tau}s + \frac{KK_p}{\tau}}$$

where:

$$K = \frac{K_c K_a K_t K_e}{K_t K_b}$$

$$\tau = \frac{RJ}{K_t K_b}$$

Comparing the denominator of this closed loop transfer function to that of a second order system:

$$\omega_n = \sqrt{\frac{KK_p}{\tau}} \quad (1)$$

$$\xi = \frac{1+KK_d}{2\sqrt{KK_p\tau}} \quad (2)$$

Transient response of a second order system :

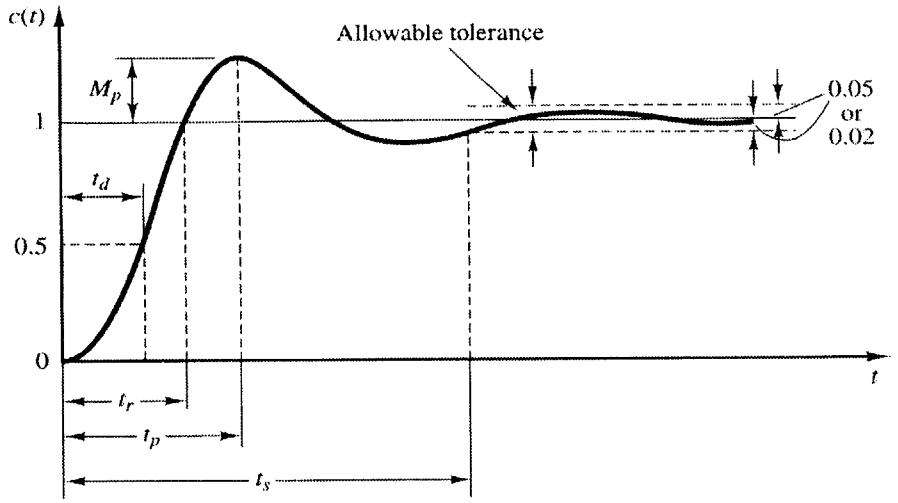

Figure 3.5 Transient response of under-damped second order system (Ogata,1997)

The under-damped system response is given as:

$$C(t) = 1 - e^{-\zeta\omega_n t}(\cos\omega_n\sqrt{1-\zeta^2}\,t + \frac{\zeta}{\sqrt{1-\zeta^2}}\sin\omega_n\sqrt{1-\zeta^2}\,t) \quad (3)$$

Maximum overshoot occurs at a peak time :

$$t_p = \frac{\pi}{\omega_n\sqrt{1-\zeta^2}} \quad (4)$$

$$M_p = C(t_p) - 1 = e^{-\frac{\zeta\pi}{\sqrt{1-\zeta^2}}} \quad (5)$$

The rise time (t_r) is obtained from $c(t_r)=1$

$$t_r = \frac{1}{\omega_n \sqrt{1-\zeta^2}} \left[\pi - \cos^{-1}(\zeta)\right] \quad (6)$$

Determining the Ki value from the full PID analysis.

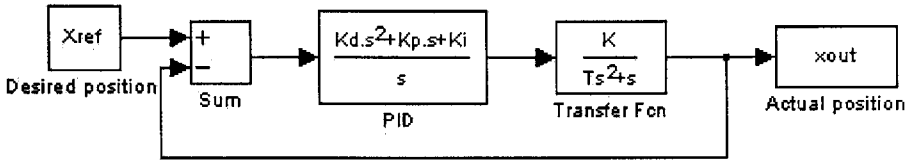

Figure 3.6 Block diagram of PID servo controller

Given the design rise time(tr) and the allowable maximum overshoot (Mp) of the system, the proportional gain (Kp) and derivative gain (Kd) can be determined. However, such systems are susceptible to steady state errors. Adding an integral (Ki) will reduce such errors. Integral gains, however, raise the order of the system by one making it a third order system, which can become unstable beyond its critical gain (Kic) value. As Ki increases, the response becomes oscillatory and the settling time increases. The critical Ki can be found using Routh's stability array analysis. Matlab® simulations of the individual stages were conducted to determine the optimum tradeoff.

3.2.1 X & Y Axes

The X and Y axes have a design rise time of 0.1 seconds and maximum overshoot of 5%. From equations (4) and (5), the system has a damping ratio(ξ) of 0.69 and natural frequency (ω_n) of 32.85 Hz. Substituting these values into equations (1) and (2), the proportional gain (Kp) is determined to be approximately 100 and derivative gain (Kd) is

determined to be 1. A Ki value of 70 was chosen based on the overshoot response of the closed loop system. Routh's stability analysis on the closed loop PID system gives a critical Kic value of approximately 5100.

A Matlab® bode plot (Figure 3.7) of the control loop gives a servo bandwidth of 30 rad/s. The 0-100% rise time of the step response is approximately 0.1 sec and the maximum overshoot is 4%, as shown in figure 3.8.

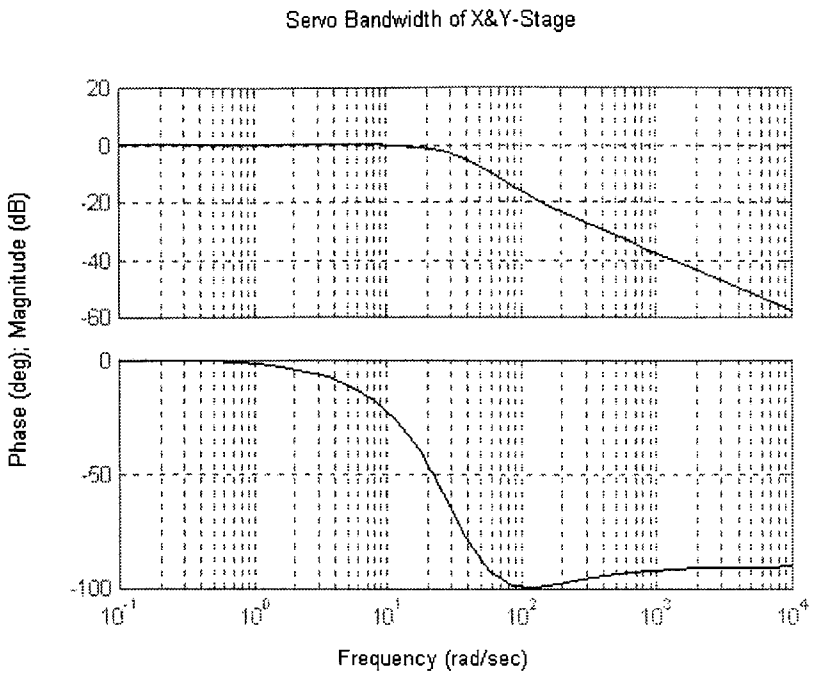

Figure 3.7 Bode plot of the closed loop transfer function of the X & Y stages

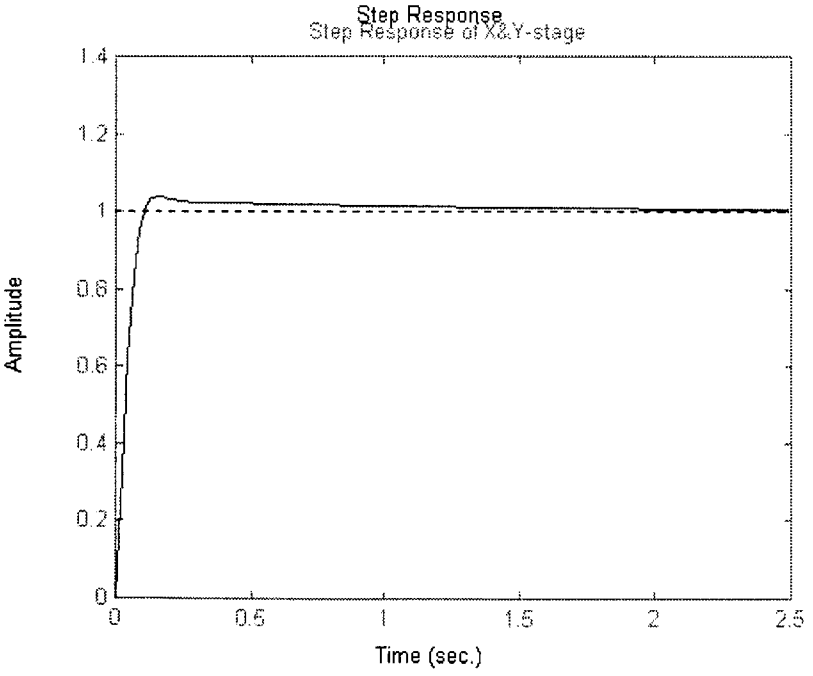

Figure 3.8 Step response of the X & Y stages

3.2.2 Z Axis

The Z-axis has a design rise time of 0.05 seconds and maximum overshoot of 5%. From equations (4) and (5), the system has a damping ratio(ξ) of 0.69 and natural frequency (ω_n) of 66 Hz. Substituting these values into equations (1) and (2), the proportional gain (Kp) is determined to be approximately 250 and derivative gain (Kd) is determined to be 3. A Ki value of 500 was chosen based on the overshoot response of the closed loop system and the disturbance rejection characteristics. Routh's stability analysis on the closed loop PID system gives a critical Kic value of approximately 26000.

A Matlab® bode plot (Figure 3.9) of the control loop gives a servo bandwidth of 70 rad/s. The 0-100% rise time of the step response is 0.05 sec and the maximum overshoot is approximately 4 %, as shown in Figure 3.10.

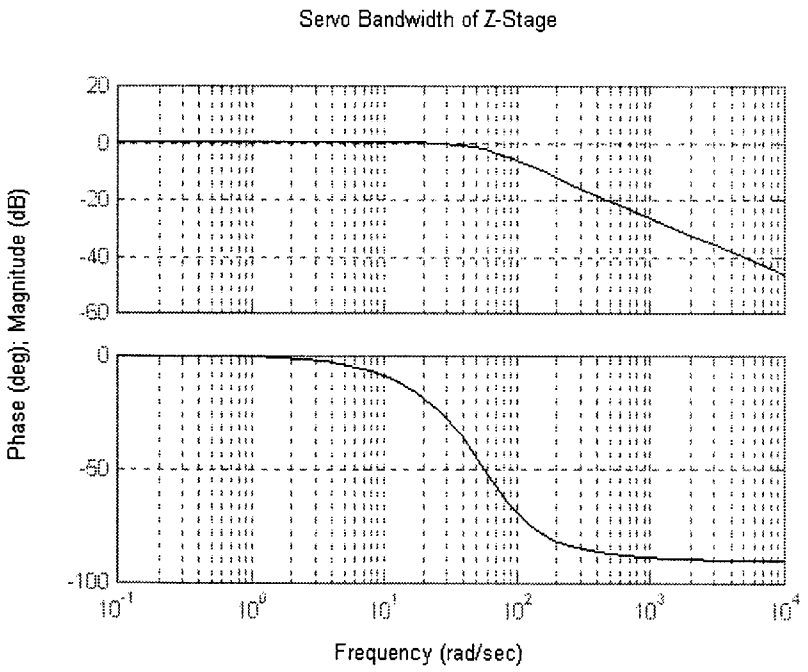

Figure 3.9 Bode plot of the closed loop Z-axis transfer function

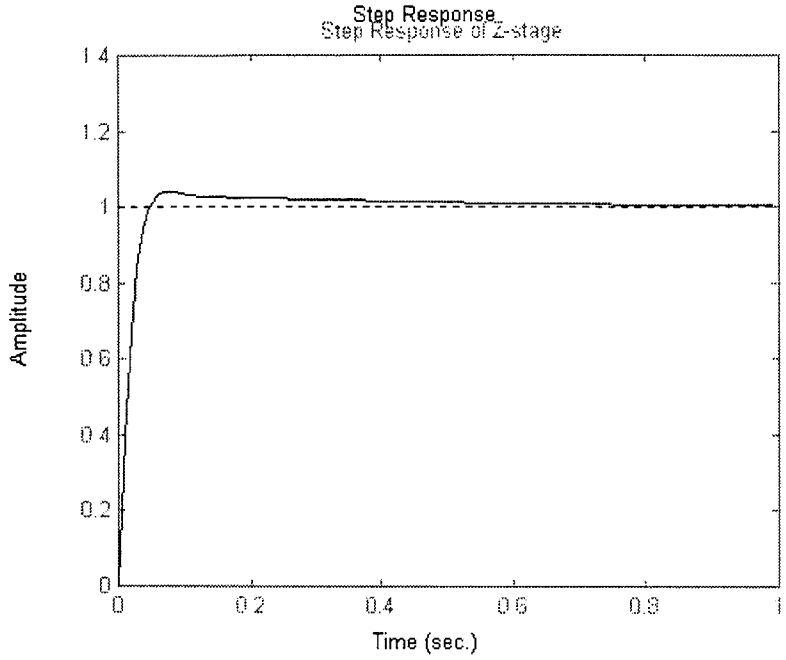

Figure 3.10 Step response of the Z-Stage

3.3 Force sensing for the Z-axis

The Z-axis is controlled through position feedback. However, the trajectory of the Z-axis is determined by the magnitude of the force exerted. A reference force is set when the program is first initialized. During scanner operation, the interrupt routine of the main controller program is constantly monitoring the LVDT displacement , which implicitly provides the actual applied force. When the applied force is equal to the desired force, the controller terminates the trapezoidal profile of the Z-axis and holds the current position. A 12 bit DAS-800 Series Keithley Metrabyte® Data Acquisition (DAQ) system is interfaced with the LVDT signal conditioner. A block diagram of the control strategy of the Z-stage is shown in Figure 3.11.

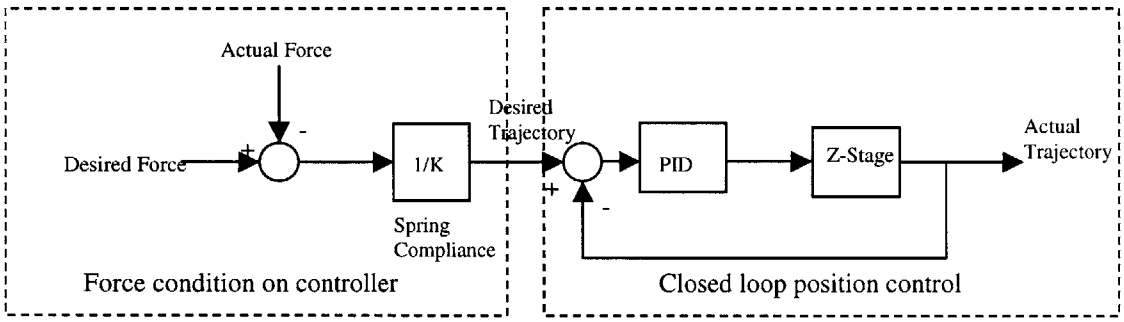

Figure 3.11 Force sensing and motion control of Z-Stage

3.3.1 System response to external load

In determining the Z-axis dynamics and control in the previous section, the drive system has been assumed to be undisturbed by external loading. However, the force sensing strategy for the Z-stage relies on the compression of a spring from external force transmitted via the laser head. The block diagram of figure 3.12 represents the servo controller with the external load represented as an effective torque experienced by the motor shaft.

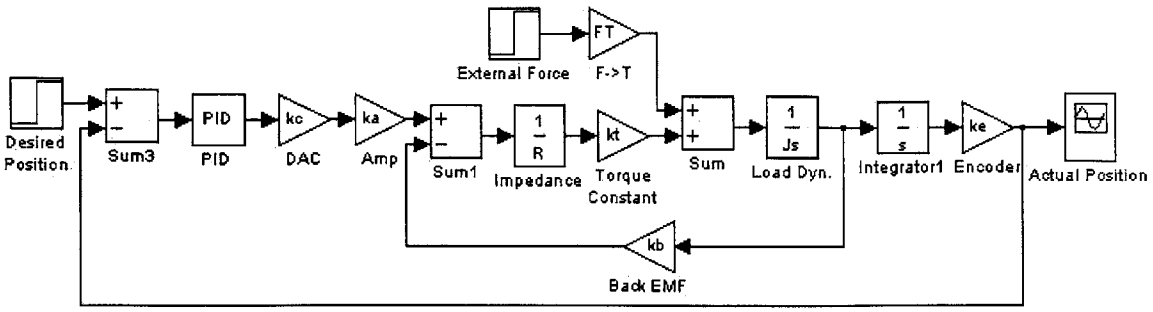

Figure 3.12 Block diagram of servo controller with external torque.

The closed loop transfer function of the system with the external load will give the same denominator as that of the undisturbed system. This means that the damping ratio and natural frequency will be unaffected. However, this disturbance torque will affect the position of the system, causing a steady state error. To improve positioning accuracy despite disturbances acting on the drive mechanism, the integral gain (Ki) of the system can be increased. The tradeoff in increasing the integral gain results is an increasingly oscillatory response and higher settling time.

The degree of disturbance rejection may be expressed by the ratio of the CL (the closed-loop transfer function between the disturbance, T and the output, xa) and OL (the feedforward transfer function between the disturbance, T and the output, xa). To improve the disturbance rejection, it is desired to make this ratio low over a wide range of frequency. Figure 3.13 shows a good disturbance rejection at frequencies of up to approximately 20Hz. Figure 3.14 shows the disturbance response (encoder counts) to a step input of 5 lbs.-force with Ki of 500. One encoder count corresponds to 0.0023 inches.

In actual operating conditions, the motor simultaneously receives an input signal position from the controller and senses an external force from the compression of the compression spring. In approximating this operating condition, a Simulink® analysis was performed with a step input position and a step force input. The step input is given a value of 200 encoder counts, which corresponds to 0.5 inches travel, and the force input is 5lb-force. Figure 3.15 shows the results of the Simulink® analysis of Figure3.12. The steady state error is approximately 2%, which corresponds to 0.01 inches. This is in the same order of magnitude as the resolution of the system and is therefore acceptable.

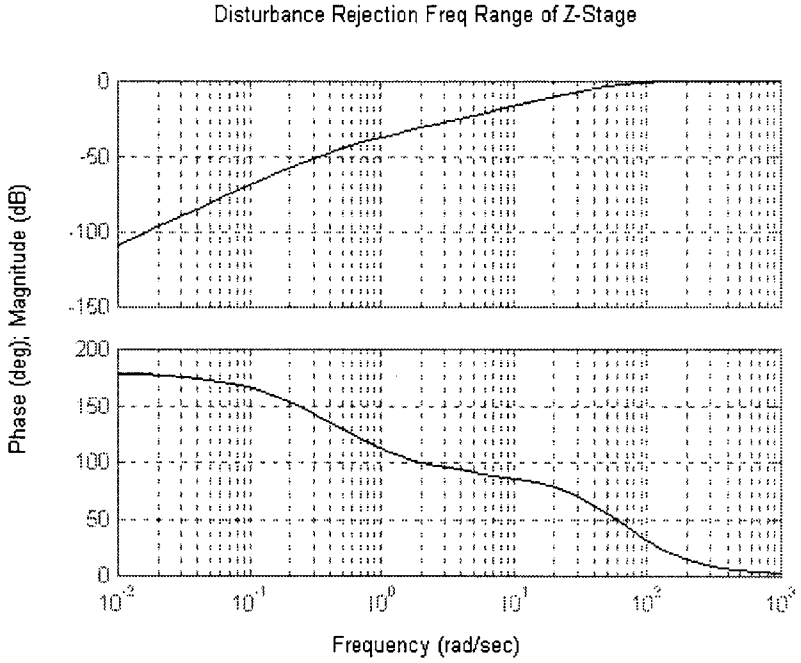

Figure 3.13 Disturbance rejection frequency range

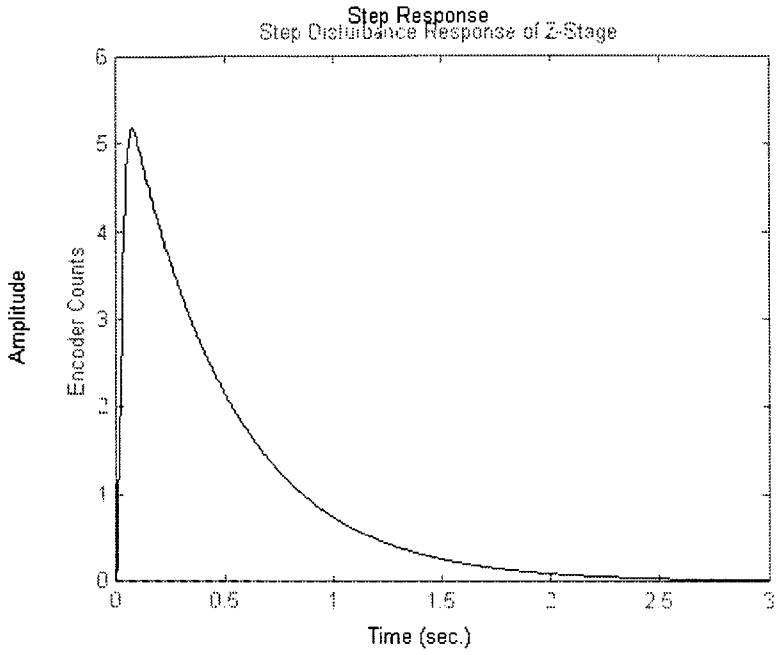

Figure 3.14 Position response to step disturbance force

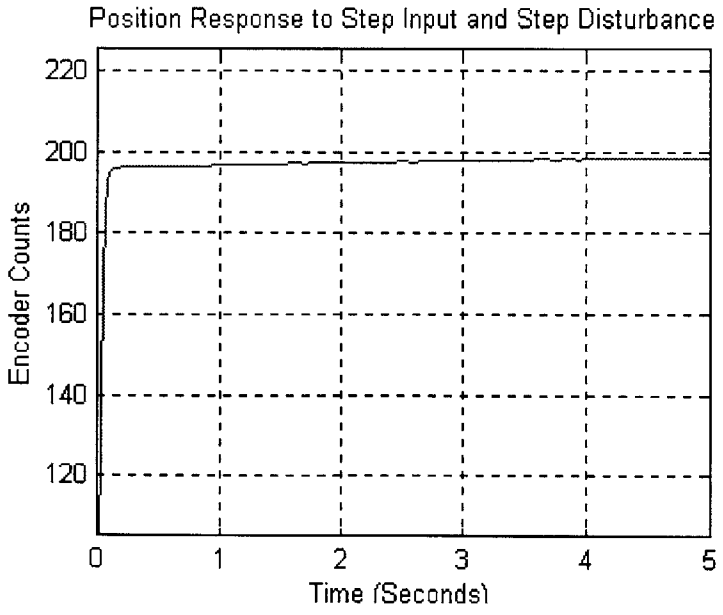

Figure 3.14 Position response to step input of 0.5 inches and step disturbance 5lbs-force

3.4 Communication between laser system and scanner

When a particular force has been achieved by the Z-stage, the main controller program would wait for a signal from the laser system to determine the next step. A triggering mechanism was designed into the controller box. This connects to the laser system through a generic BNC cable. A 3 msecs pulse triggers the E2000^{TM} system at each scanner cycle that occurs every one second. The interrupt routine in the controller program samples the DAQ channels at 6 msecs . For the board to sense the laser pulse, the time delay from the trigger was increased using a capacitor and resistor placed in parallel across the trigger input. A 1 kΩ resistor and 1μF capacitor are used to magnify the time delay. The electrical schematic of the trigger mechanism is given in Figure 3.15.

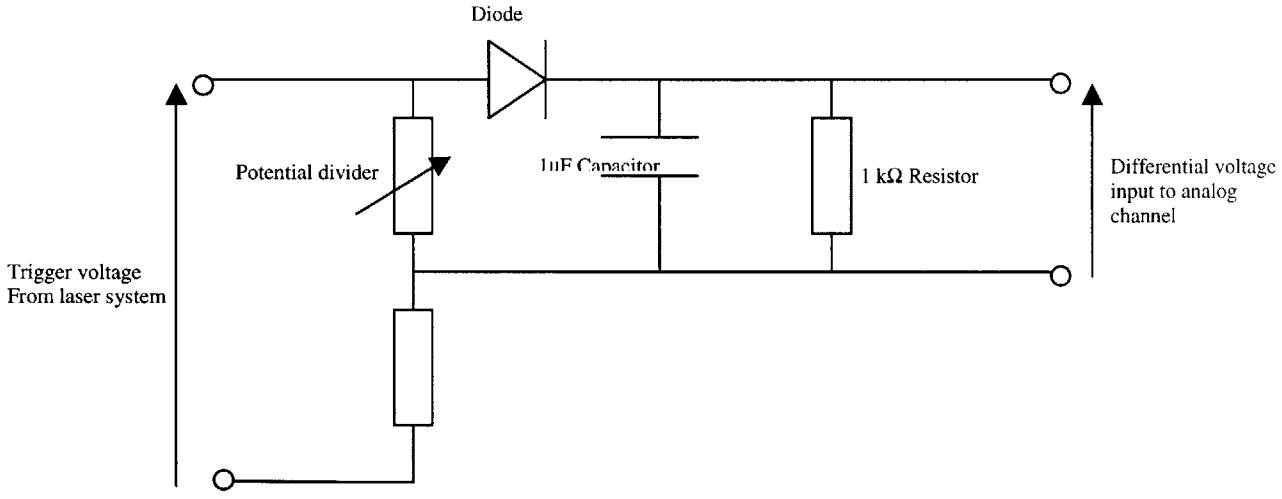

Figure 3.15 Electrical schematic of trigger mechanism

3.5 User Interface

To control the scanner variables, a user interface was designed. This allows the operator to change the total scan area, step sizes of the X and Y stages, the velocity of the three axes and the applied force in the Z-direction. The controller was written in the C programming language.

To provide flexibility, most of the cues and parameters to the motors can be easily changed . This is necessary to find the critical variables for the different applications. Once the variables are found, the program can be easily customized for the operator and application. The controller code reads the input parameters from a data file. This made the program more user friendly and manageable.

In addition to software controls, there is a button positioned strategically on each of the scanner's handle. One acts as on/off button for the scanner motion while the other serves as an emergency stop button that immediately cuts off all power supply to the electronic controller box.

4 Experimentation with MIT/MI Scanner

Prior to shipment, performance tests conducted at MIT/MI showed that almost all functional requirements of the scanner, shown in Figure 4.1, were met. The mechanical performance of the three-axes is presented in this chapter, and finally, suggestions are made for future improvements to the scanner.

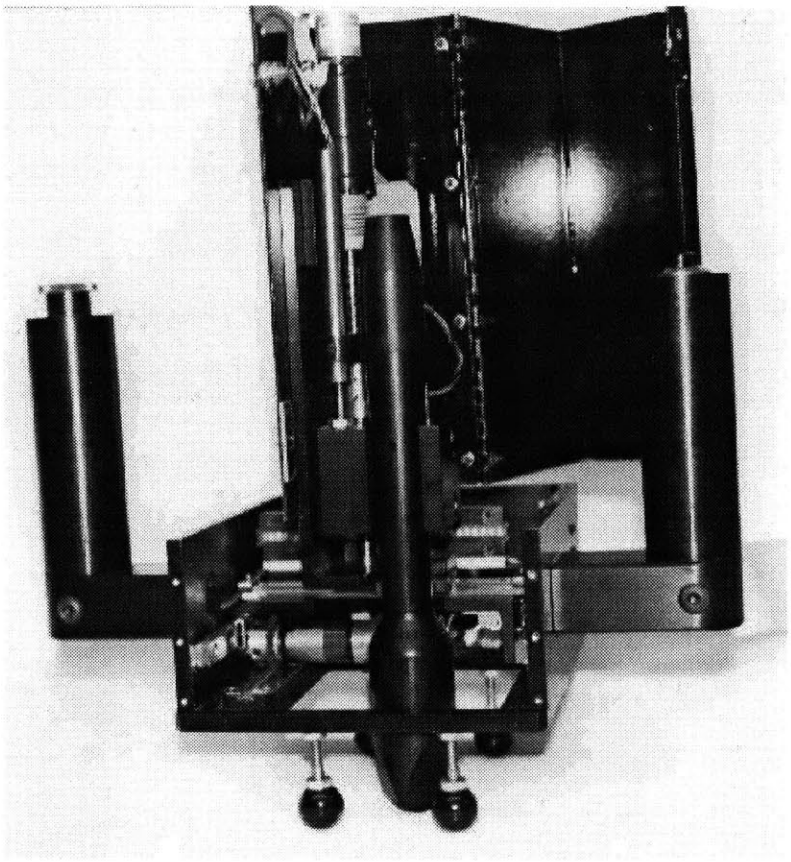

Figure 4.1 MIT/MI Automated Scanner

4.1 X-Axis Performance

The maximum scan range of the X-axis is 2.5 inches, ½ inch more than the minimum requirement. This is more than compensated by the fact that the machine can be easily handled and moved to the next scan area. The scan range can be easily changed in the user interface. The resolution of the stage is 0.002 inches, a factor of five less than the designed 0.01 inches. However, the choice of a rack and pinion drive and planetary gearhead on the motors introduces a combined backlash error of +/-0.005 inches. The dynamic response of the system proves satisfactory when the modeled parameters are used. Response data obtained from a step input of 0.2 inches gives a 0-100% rise time of 0.084 seconds. Figure 4.2 shows a maximum overshoot of 4.24%. Recall that the designed rise time is 0.1 seconds with a maximum overshoot of 5%. Figures 4.3 and 4.4 show the final X-axis set-up and the bottom view of the scanner, respectively.

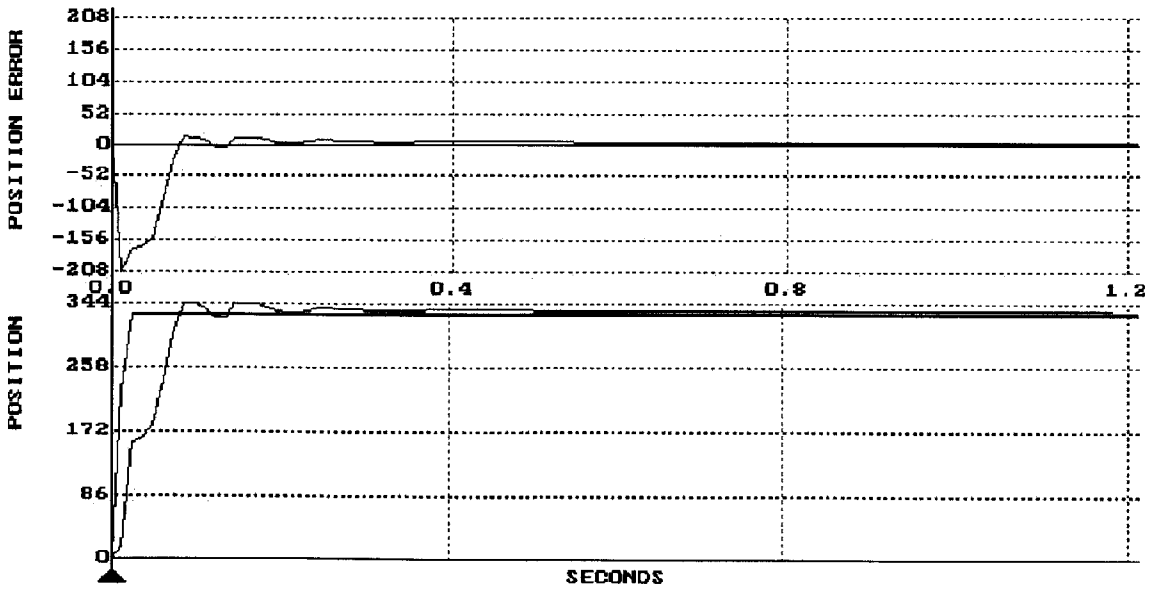

Figure 4.2 Step response of X-axis

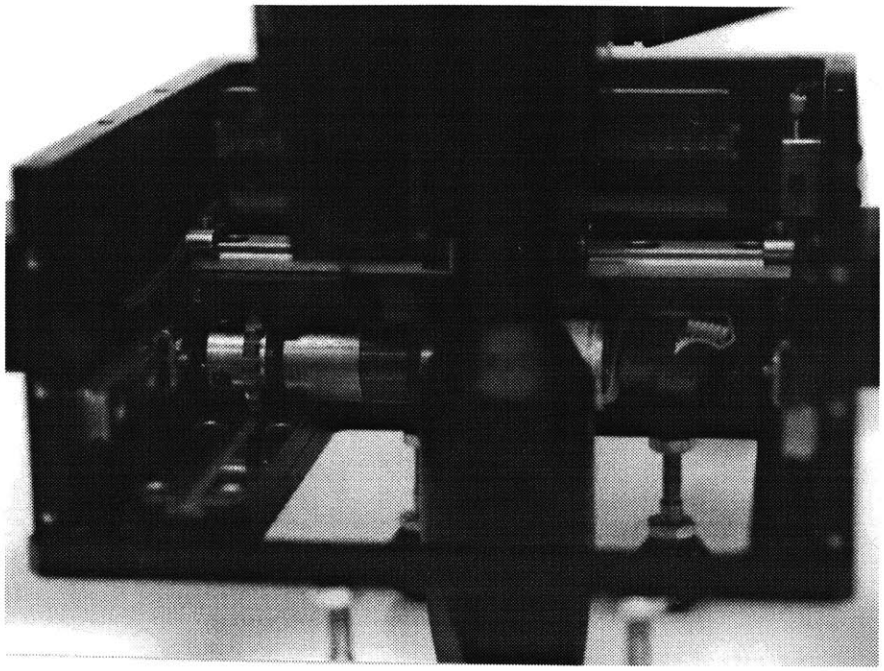

Figure 4.3 X-Stage of Scanner with EpiWand® in foreground

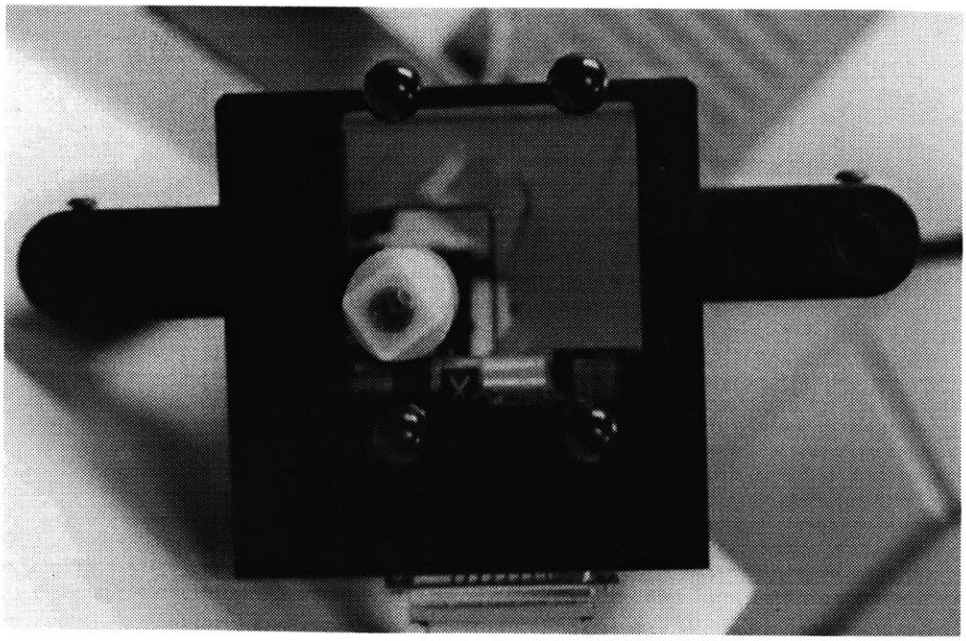

Figure 4.4 Bottom View showing the sapphire tip located in the X&Y-axes scan area

4.2 Y-Axis Performance

The maximum scan range of the axis meets the specifications of 2 inches. As mentioned earlier, this is compensated by the ease of moving the machine to the next scan area. The actual range is longer than 2 inches, but due to internal wiring and cabling, it was suggested that some space allowance be allocated. The Y-stage has a motor with a 43:1 gearhead connected on a 0.8324 inches diameter pinion. The tradeoff of such an assembly is the +/-0.005 inches backlash. Nevertheless this was still within the limits of the design requirement of 0.01 inches. When the motor is given a step input of 0.2 inches, the dynamic response gives a 0-100% rise time of 0.092 seconds and maximum overshoot of 9.09% (Figure 4.5). The rise time is lower than the designed 0.1 seconds response but the overshoot exceeds the 5 % limit.

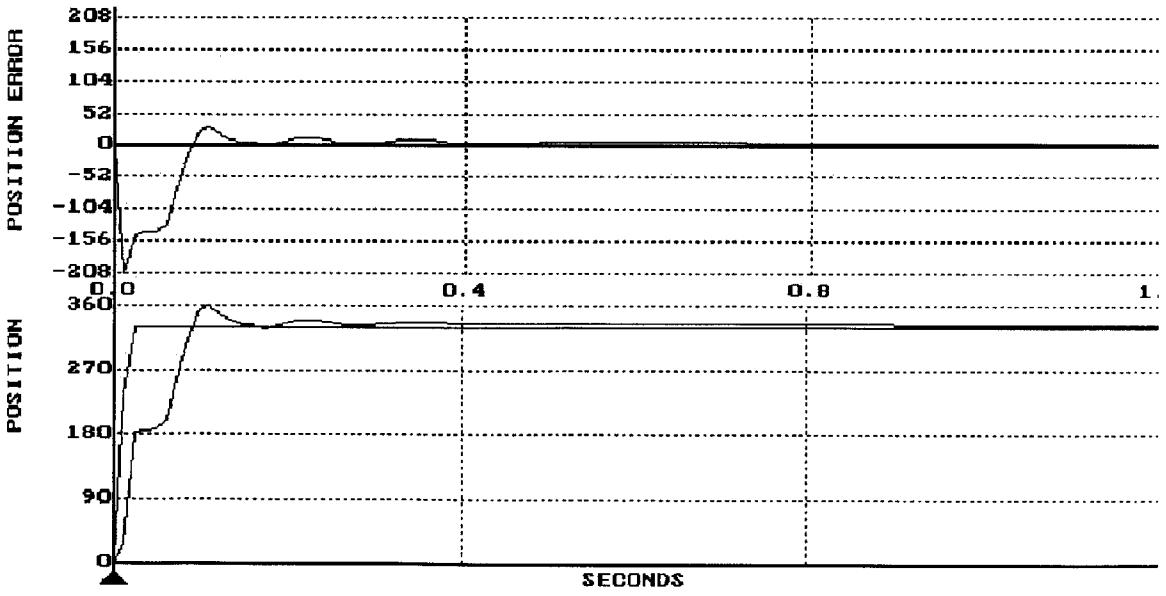

Figure 4.5 Step response of Y-axis

4.3 Z-Stage Performance

The full range of the Z-stage, with the laser hand-piece attached, is approximately equal to the design stroke of ¾ inches. The resolution of the direct drive ballscrew actuator of 0.0023 inches is better than the functional requirement of 0.004 inches. The system under-performed in the dynamic response test when driven with the modeled parameters. Actual response to a step input of ½ inches gives a 0-100% rise time of 0.056 seconds and an overshoot of 8.5%, as shown in Figure 4.6. This is slightly below the design response of 0.05 seconds and 5% overshoot. However, this is an acceptable compromise given the good performance of the disturbance rejection response to a force input of 5 lbs., as shown in Figure 4.7. The actual steady state error is reduced to less than 1% after 0.8 seconds compared to a 3 seconds in the designed system shown in Figure 3.14 of the previous chapter. The integral gain can be reduced to improve the dynamic response but that would result in a higher steady state error.

The force sensor works better than initially expected. The noise interference in the 12 feet cabling between the LVDT and the signal conditioner is minimal. Calibration tests conducted on the LVDT signal output provided a good linear relationship to the force in the constant-stiffness spring. Replacing springs of different stiffness easily changes the force range. The use of a compliant spring increases the resolution of the sensor and improves the dynamic stability of the system. Figure 4.8 shows the Z-stage force detection system.

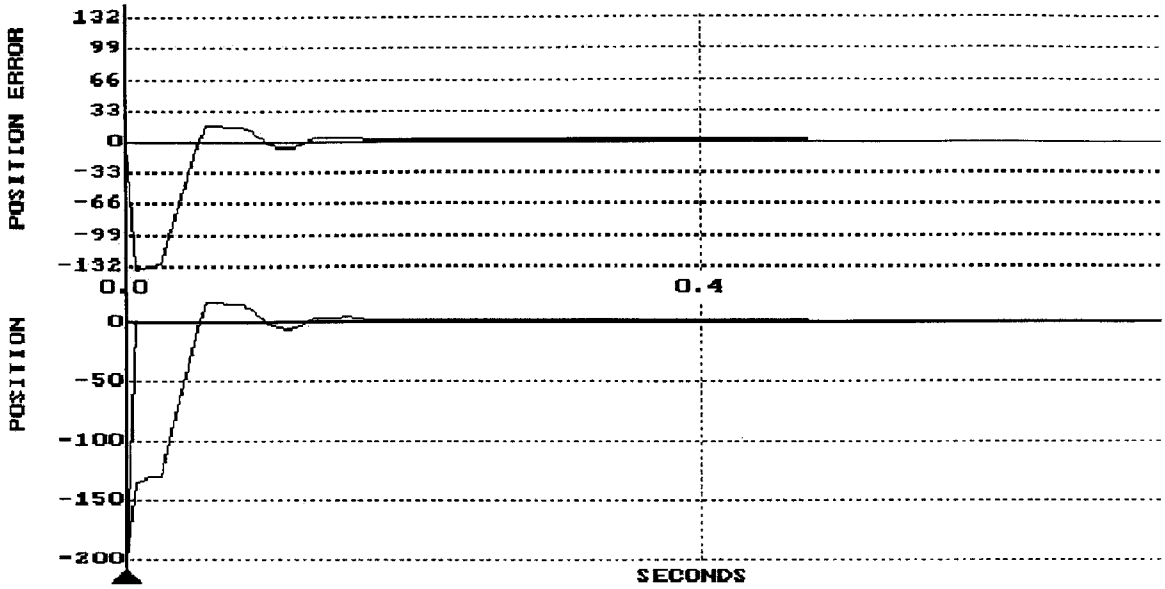

Figure 4.6 Step response of Z-stage

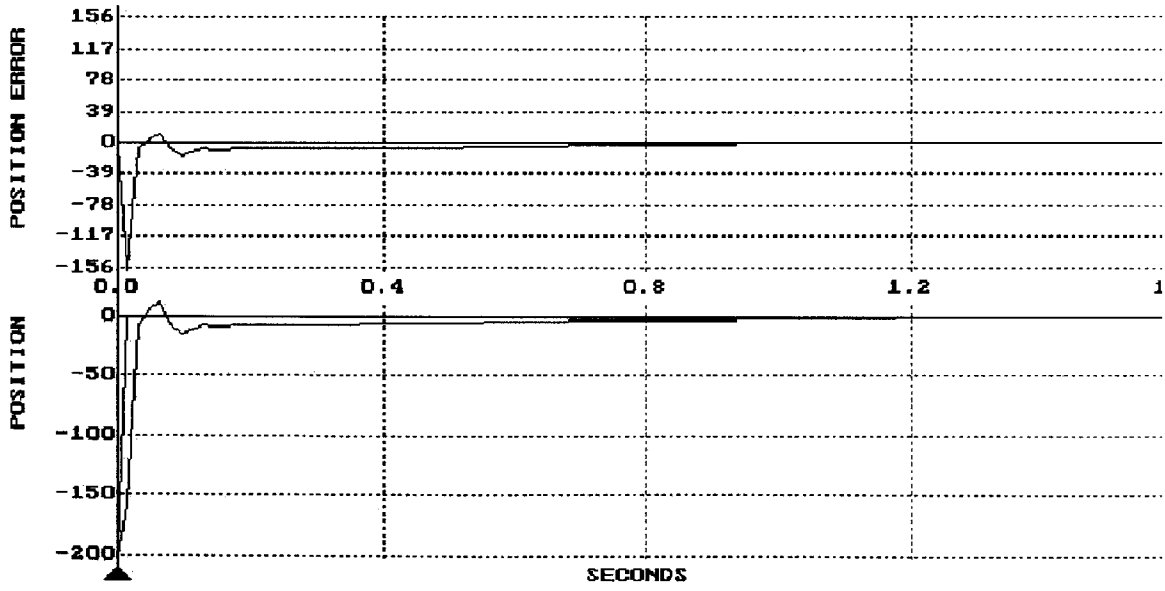

Figure 4.7 Response of Z-stage to step position and step disturbance

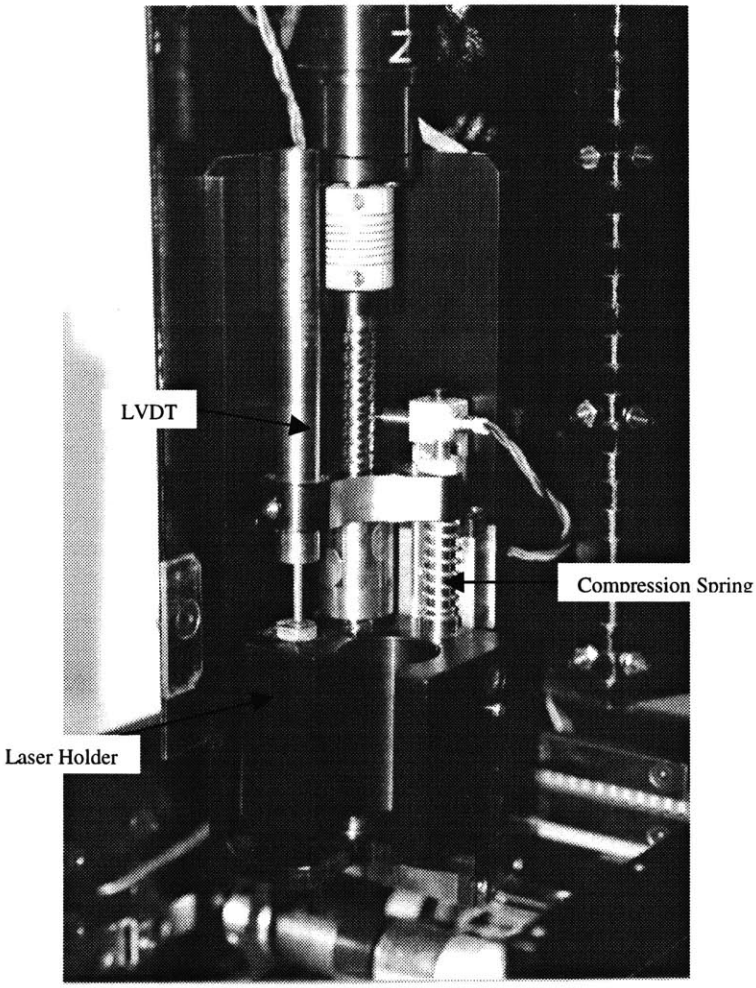

Figure 4.8 Z-Stage force detection system

4.4 Scanner-Laser Interaction Performance

This section provides a report on the interaction performance of the scanner-laser system. Figure 4.9 shows the E2000^{TM} system interfaced with the scanner. Clinical results are discussed in the conclusion chapter. The rapid rise time designed for all three axes resulted in high torques generated in the individual motors. At many instances, the counter-moments induced in the handheld scanner frame made it unwieldy. To reduce this effect, the motor was driven at a slower speed.

The rise time of the X and Y axes were reduced to approximately 0.16 seconds and the Z-axis to 0.15 seconds. Clinical test showed that the reduction of speed in the Z-stage has beneficial effects in terms of patient comfort. The laser hand-piece is brought down to the skin at a lower acceleration causing less discomfort. However, the speed cannot be reduced significantly as the thermocouple on the laser hand-piece requires a certain rate of change in temperature to achieve firing condition as it makes contact with the skin. The combined step time of all three axes during one cycle is still sub-1 second. This was facilitated by the effective laser-scanner communication system. The pulse triggering communication system improves the overall coordination process, thus allowing a more efficient operation. This enables the system to move on to the next cycle as soon as the laser has been initiated for the current cycle.

The scanner has some difficulty in skin contours that have high curvature. In such instances, the laser head approaches the skin at an oblique angle causing difficulties in laser initiation. This is the main limitation of the scanner. When the triggering mechanism does not sense the laser pulse within 0.5 seconds in the bottom position, the controller pulls the Z-stage up and holds it to allow the sapphire tip to cool down. The

scanner then lowers the hand-piece down again on the same spot. The laser system usually fires by the second try. In situations where the laser does not initiate after several repeated cycles, the user interface allows the operator to intervene. This ensures that no spot goes unfired. It is proposed that a swiveling head be included in the design of the next version. This would ensure that the laser hand-piece approaches the skin perpendicularly. Due to the space limitations in the current system, this feature was deliberately omitted.

The total weight of the machine is about 5 lbs. This gives a good compromise between ease of handling and counter-weight for the force application process that tends to lift the scanner off the surface. Figure 4.10 shows that the relative size of the scanner with respect to an operator. Polymer and other composite modern materials can be used for additional reduction in weight. However, it would be important to keep a considerable mass on the system for the reason specified above.

As a means of improving the performance of the system, it is highly desirable to obtain the relative velocity between the laser hand-piece and the skin surface. As the skin has elastic characteristics, this proves to be a problem especially with conventional speed sensor devices. This is the main motivation for the next phase of the project and will be discussed in-depth in the next chapter.

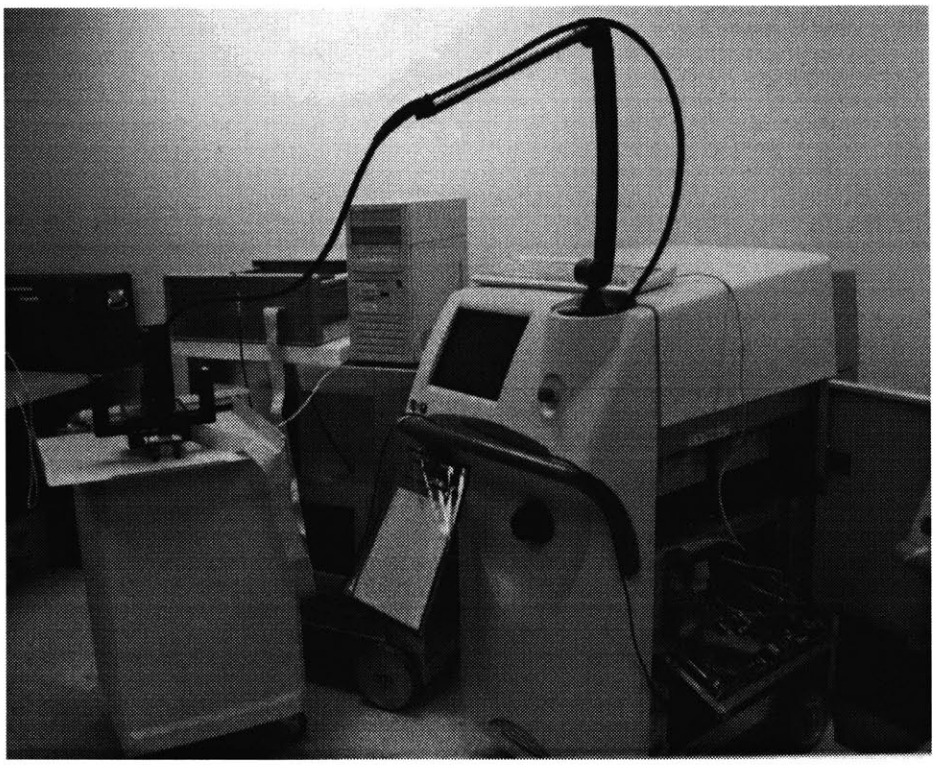

Figure 4.9 E2000™ system interfaced with the MIT/MI Scanner

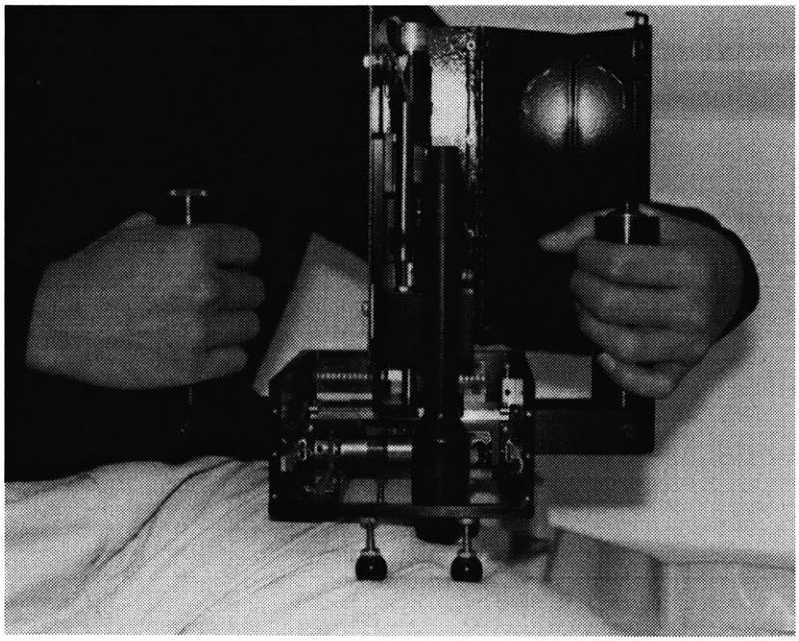

Figure 4.10 Scanner easily manipulated by human operator

5 Velocity Sensor

Clinical tests of the scanner have shown that the velocity readings obtained from the differentiated position counts at the motor encoders, often times do not correspond to actual relative velocity between the laser hand-piece and skin. This is true especially in cases when the laser probe is dragged across the skin surface with an applied downward force. This is due to the elastic behavior of human dermis. As illustrated in Figure5.1, the initial position of the hand-piece is above elements 5 and 6. When dragged with a velocity, V, along the surface, the hand-piece is still above elements 5 and 6.

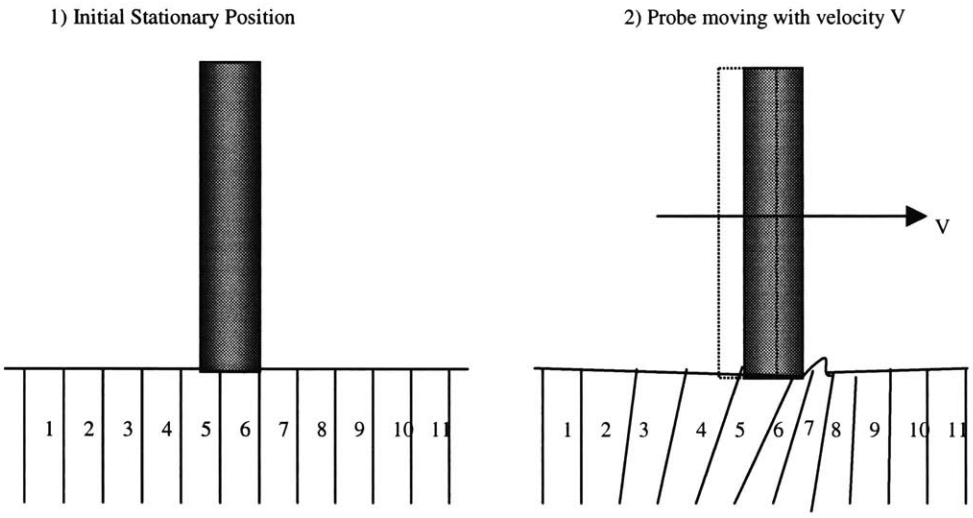

Figure 5.1Illustration of the elastic behaviour of skin

Adjusting the scanner's working parameters in real-time will increase the interaction performance of the scanner-laser system with the skin. The current set-up only allows communication between the laser system and the scanner. It is desirable to obtain actual real time information of the laser-skin interaction. This enables on-the-fly changes of scanner working parameters that will in turn affect the laser system. Subsequently, this

will alter the laser-skin interaction and optimum working conditions can be achieved . The second phase of the project involved experimentation with various velocity sensing mechanisms on the market. Some new methods of sensing velocity were also proposed and experimented with.

Another motivation for direct velocity sensing is to increase the control performance of the scanner. Full state feedback systems often require velocity feedback in order to obtain a clean low-noise velocity signal. In practice, however, not all state variables are available for feedback. It is important to avoid differentiating a state variable to generate another one. Differentiating a position signal to obtain a velocity signal often leads to noise spikes, unless the position sensor's resolution is about 10 times greater than the required mechanical resolution.

5.1 Functional Requirements and Constraints

There were a number of functional requirements that had to be met in the design of the velocity sensor. Cost was deliberately minimized, as the sensor forms a peripheral component to the scanner assembly. The functional requirements are given below:

1. Direct measurement of relative velocity between laser hand-piece and skin along one axis.
2. Non-marking of skin surface
3. Compact design with footprint of 1.25 inches by 1 inch and height of 2 inches.
4. Minimum resolutions of 0.01 inches/sec
5. Maximum response time of 100 msecs

The first requirement is the most important as this would provide actual relative velocity data that is crucial in the laser-skin interaction. There is a plethora of velocity sensor products out on the market but most are unsuitable for the current application, especially systems that rely on a base reference frame. This includes generic interferometric devices, magnetic trackers, linear encoders, potentiometers, LVDTs and proximity sensors. This is due to the elastic behavior of human skin. The sensor should only be sensitive along one axis.

The second requirement is important to avoid contamination of the skin surface. Some velocity sensors have photodetectors that read the equally spaced markings on a surface to obtain velocity readings. This is analogous to stripe markings for bar-code readers. This could be achieved by projecting black-white graduations or dispensing colored marking agents at regular intervals across the length of the interested surface.

Prior to E2000™ treatment, the skin is cleaned and treated with a conditioning agent that ensures proper surface conditions. Introduction of a foreign colored marking agent could contaminate the primer and create a potentially hazardous situation. The markers will absorb the high-energy laser light, causing excessive overheating of the adjacent skin.

The third requirement limits the use of bulky velocity sensor equipment. The work volume is derived from the allowable free space adjacent to the laser hand-piece. Due to the limited space between the laser hand-piece and the scanner, this work volume is kept to a minimum.

The fourth requirement sets the performance specification of the system. To make real time system parameter adjustments, it is desirable to have a detector with high resolution. Systems with low resolution can create operation problems, as the wide fluctuations in output will affect the controller performance. As mentioned earlier, a low-resolution position feedback system will introduce noise spikes when the signal is differentiated to obtain velocity readings.

The final specification sets the controller response to changes in velocity. Large delays would create operational difficulties, especially in coordinating the scanner with the laser-skin performance. The system will not have enough time to respond accordingly. The optimal pulse duration for photothermolysis is less than or equal to the thermal relaxation time (TRT). The TRT for the skin follicles (200 to 300μm diameter) is approximately 40 to 100 msec [Grossman et al, 1996]. For the scanner system to adjust its parameters within the allowable TRT limit, the velocity controller has to have a maximum response time of 100msec.

5.2 Rotary Encoder Based Velocity Sensor

5.2.1 System design

The rotary encoder based system is very straightforward and relies on a series of timing pulleys and a belt to rotate the encoder shaft. The limiting dimension of this set-up was 1 inch as stipulated by the third requirement. Therefore timing pulleys of equal or smaller diameters had to be used. The minimum pitch diameter of timing pulleys manufactured was found to be approximately ¼ inches. Coupled to a larger 1-inch diameter pulley, this gives a maximum 1:4 ratio. To obtain a resolution of 0.01 inches, the encoder has to have a minimum of 80 counts per revolution.

Most miniature PC mountable encoders range from 24 to 50 counts after quadrature. This necessitated the use of larger encoders, and a Bourns® EN series rotary encoder of 128 pulses per revolution (PPR) was chosen as a good compromise between size and resolution. The high PPR allowed the use of smaller timing pulleys in the final design .A 0.255 P.D and a 0.407 PD timing pulley coupled through a 1/8 width belt were used as shown in Figure 5.1. A spur gear was added to provide grip on the skin surface. This is necessary, as the surface of the skin is pre-treated with an oil-based lotion.

The encoder was connected to a Nulogic© motion controller board that provided the quadrature output to a LabVIEW ® graphical control panel. The position counts were differentiated to obtain the velocity output.

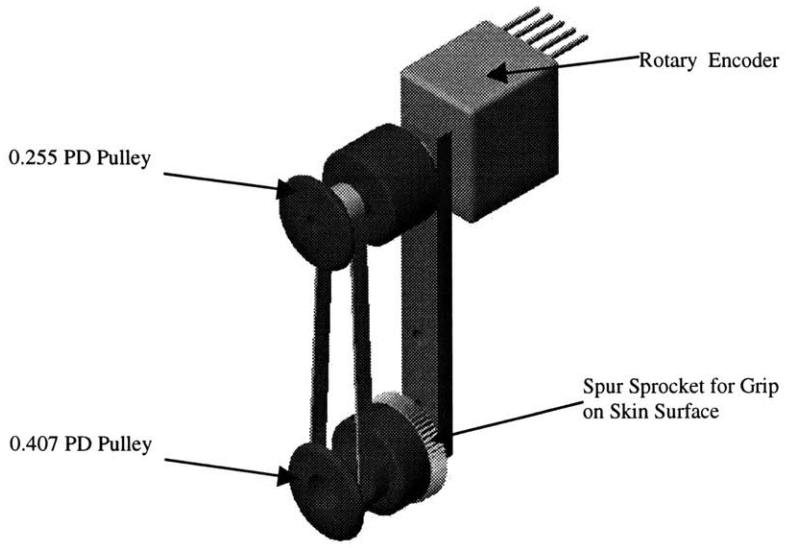

Figure 5.1 Encoder based velocity sensor

5.2.2 Experimental Results

There are two methods of differentiating position counts to obtain velocity. The first method counts the numbers of encoder counts between synchronized time steps. The second relies on the measured time between pulses. Both approaches were taken and the latter method yielded superior velocity response. The first method provided a noisy output especially at low speeds. Large errors can result if only one or two encoder tics go by within the fixed loop time. The second method provided higher accuracy and less noise but its performance depends on the resolution of the time steps.

The encoder position counts are digital and are not prone to external noise signals unlike regular tachometer systems which produce analog signals. However, the total size of the encoder-based velocity sensor was still relatively large and this was limited by the off-the-shelf low-cost encoder systems available.

5.3 Accelerometer-Based Velocity Sensor

5.3.1 System Design

The main advantages of the accelerometer based velocity sensor are its simple design and ease of maintenance due to the lack of moving parts. The system also utilizes a snap-acting switch that is in constant contact with the skin to take into consideration the elastic behavior of skin. When there is relative motion between the skin and sensor, the lever arm will close the switch and the velocity readings will be taken. An Analog Devices® ADXL05EM-1 was chosen for its low cost and ease of use. No additional active components are required to interface with the Keithley Metrabyte® DAS800 DAQ. A LabVIEW ® graphical interface was written to integrate the acceleration signals to velocity.

The ADXL05EM-1 is a single monolithic integrated circuit forced balanced capacitive sensor. It can measure both AC accelerations (typical of vibration) or DC accelerations (such as inertial force or gravity). Piezoresistive devices are less precise and more expensive. Instrumentation piezoelectric accelerometers start at $500. Figure 5.2 illustrates the accelerometer mounted on a bracket adjacent to the snap-acting switch.

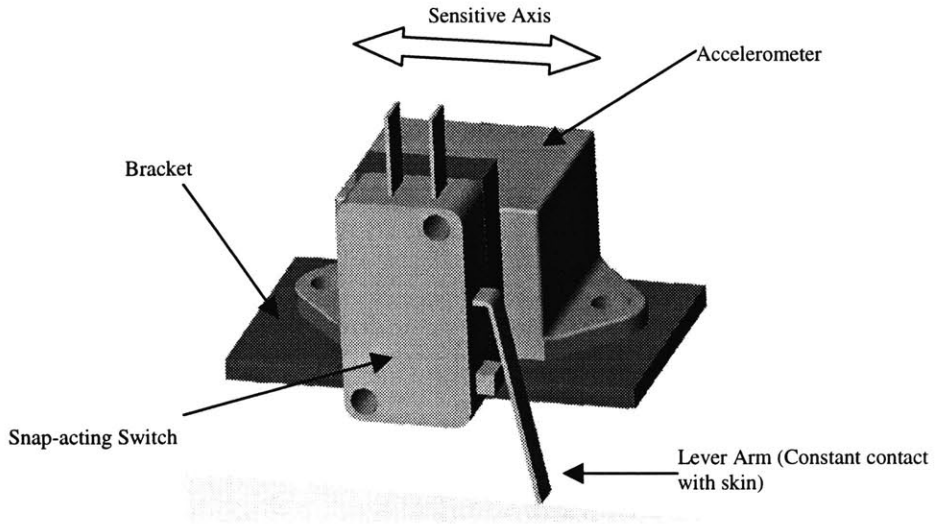

Figure 5.2 Accelerometer-based velocity sensor

5.3.2 Experimental Results

The acceleration signal was integrated to obtain velocity readings A linear belt drive system of varying velocities was used to calibrate the accelerometer unit. Noise corruption from the environment could be filtered using low pass filters. The biggest errors however came from the gravitational (inertial) vector due to tilt of the unit and thermal drift of the sensor. Accelerometers are also susceptible to errors caused by cross-axis motion on the order of 0.002g/g. To avoid inertial effect errors; the unit had to be mounted horizontally. This created problems in situations where the scanner was tilted when located on a curved surface. Costlier piezoelectric accelerometers, which are only sensitive to AC vibrations, can also be used to avoid inertial problems. Accelerometers aligned in a Rosette configuration, along the three different axes, will compensate for drift and cross-axis motion errors. This however, will make the unit bulkier and will create mounting difficulties as the units have to be orthogonal to one another.

5.4 Miniature Tachometer

A tachometer is the rotary form of a velocity transducer and the most common form is a DC tachometer. Rotation of the armature (wound rotor) across the permanent magnet stator field induces voltage in the armature that is proportional to the rotation speed. The voltage is then carried through the commutator to the output terminals. DC tachometers essentially operate as reverse DC motors. Common tachometer dimensions start from diameters of 4/5 inches with lengths of 1.5 inches and cost anywhere from $150 for basic units to $1000 for high performance units [Slocum,1992]. These limited the use common tachometers in the current application due to size and cost constraints.

As a result, an intensive literature search was conducted into miniature permanent magnet DC motors on the market. Namiki® miniature vibrator motors (4.2CH-1001NL-00) were chosen for their size and cost. To detect the low back electromagnetic force (emf) (50μV/rpm) generated by the motors, a 16-bit National Instruments® DAQ (ATMIO 16XE-50) at settings of +/-100 mV was used. The motors have a diameter of 4.2 mm and are originally designed as internal vibrator motors for pagers. A ½ inch wheel was attached to the end of the motor shaft. To achieve resolutions of 0.01 inch/sec, the wheel would rotate at 0.4 rpm and induce approximate 20 μV back emf. This was well within the resolution of the DAQ system.

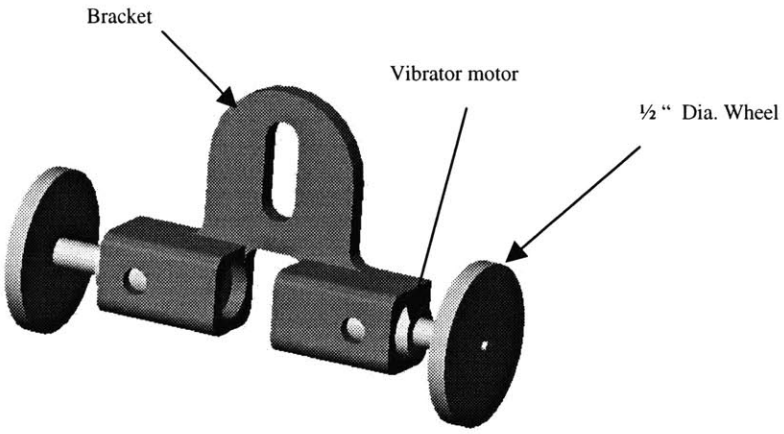

Figure 5.3 Tachometer-based velocity sensor

5.4.1 Experimental Results

Ideally, the back emf from the DC motor should provide a pure DC voltage that is proportional to the angular rotation. However, the output has a pulsating characteristic, known as ripples, due to the discrete number of armature coils. The ripple effect is caused by the net output tracing the peak voltage of the different coils, as illustrated in Figure 5.4

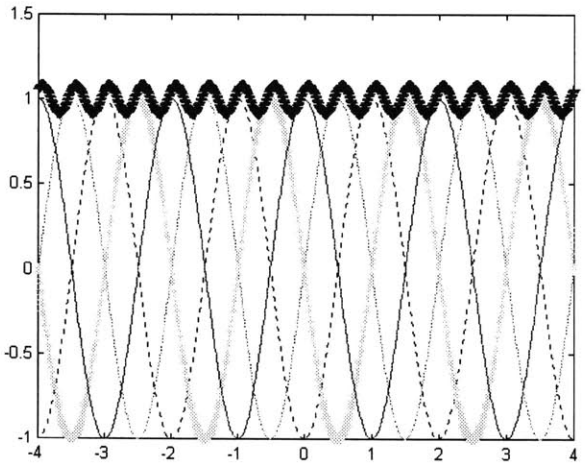

Figure 5.4 Rippled back emf output from a four armature coil motor

There was also significant noise interference in the low voltage analog output. The ripples effect can be reduced using filtering techniques or by increasing the number of coils. Changing the number of coils, however, is not a viable option. Low pass filters are an effective means of reducing both the ripple and noise but they add time-delays to signal processing loop. Digital filtering was chosen over op-amp active filters to reduce the number of peripheral drive electronics and limit the size of the tachometer unit. However, the low DC analog signal of the tachometer is more susceptible to noise in the cabling to the DAQ board.

Passband is the region of the frequencies that are relatively unattenuated by the low pass filter. This region is usually defined to the –3dB point. Stopband lies at the bottom of the transition region, where there is significant attenuation. In designing low pass filters, three criteria should be considered. The first is the sharp transition from the passband to the stopband. The second is the amount of ripple allowed in the passband. Finally, the ability of the filter to pass signals within the passband without distortion of the waveforms caused by phase shifts. There are three popular low pass filters; Butterworth filters (maximum flat passband), Chebyshev filters (steepest transition from passband to stopband) and the Bessel filters (maximally flat time delay).

To determine the best low pass filter for this application, data from a step velocity input was sampled at 100 Hz for 3 seconds. A Matlab® analysis was performed using the three filtering strategies using filter parameters of a1 Hz passband and a 4 Hz stopband with no more than 10 dB loses in the passband and with at least 16 dB of attenuation in the stopband. The results of the simulation are given in Figure 5.5.

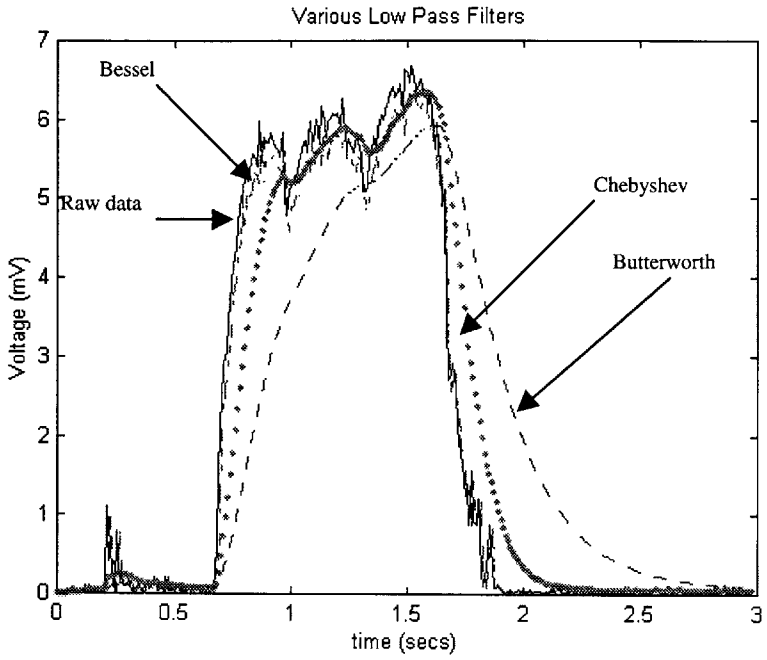

Figure 5.5 Comparison of the three main low pass filters

The Bessel response has the best possible time delay but does not effectively filter out the higher frequencies due to its droopy passband and gradual falloff profile. The response time is approximately 20 msecs. The Chebyshev filters gave the best overall performance with significant filtering of the higher frequencies and time response of approximately 120 msecs. The ripple was limited to 0.5 dB. The Butterworth gave the smoothest response with effective filtering, however, the time response of 300 msecs was not acceptable.

A second order Chebyshev low pass filter was chosen as the filter for the system. Higher order filters provided better attenuation but introduced longer time delays as illustrated in Figure5.6.

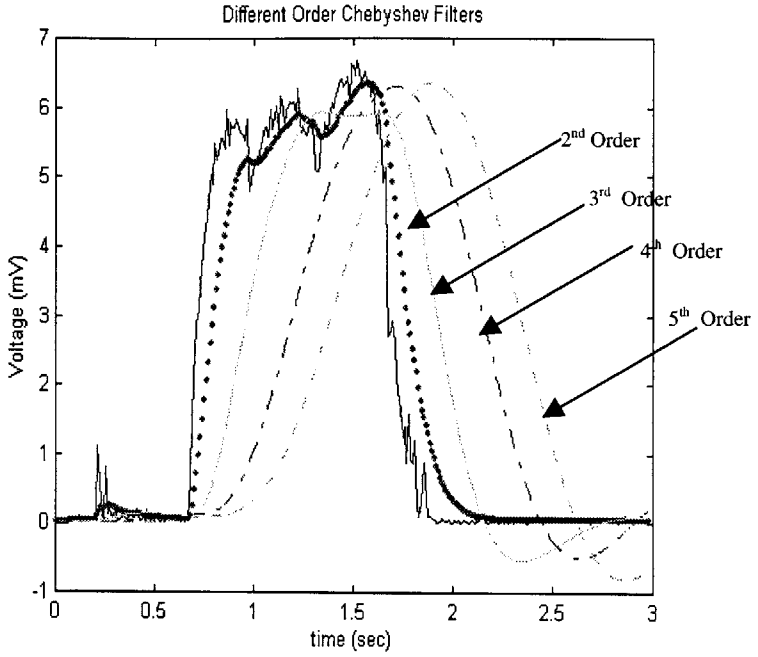

Figure 5.6 Comparison of performance of the different order Chebyshevs

A LabVIEW ® routine was written to provide real time filtering and calculation of the tachometer output. To compensate for the time delay added by the Chebyshev filter, an extra routine was added to analyze the raw data. A flag is sent to the main controller whenever the velocity dropped below a threshold value. This improved the performance with an approximate time response of 50 msecs. The noise in the signal provided a fluctuation of +/-0.004 inches/sec. This creates a resolution of 0.008 inches/sec which is within the functional requirement of 0.01 inches/sec. Higher order filtering techniques can be employed with an added time-delay penalty. The overall system performance was satisfactory considering the size of the tachometer unit. The tachometer provided a smooth linear relationship between velocity and induced back emf, as shown in Figure 5.7. A linear belt drive of known velocity was used to calibrate the tachometer unit.

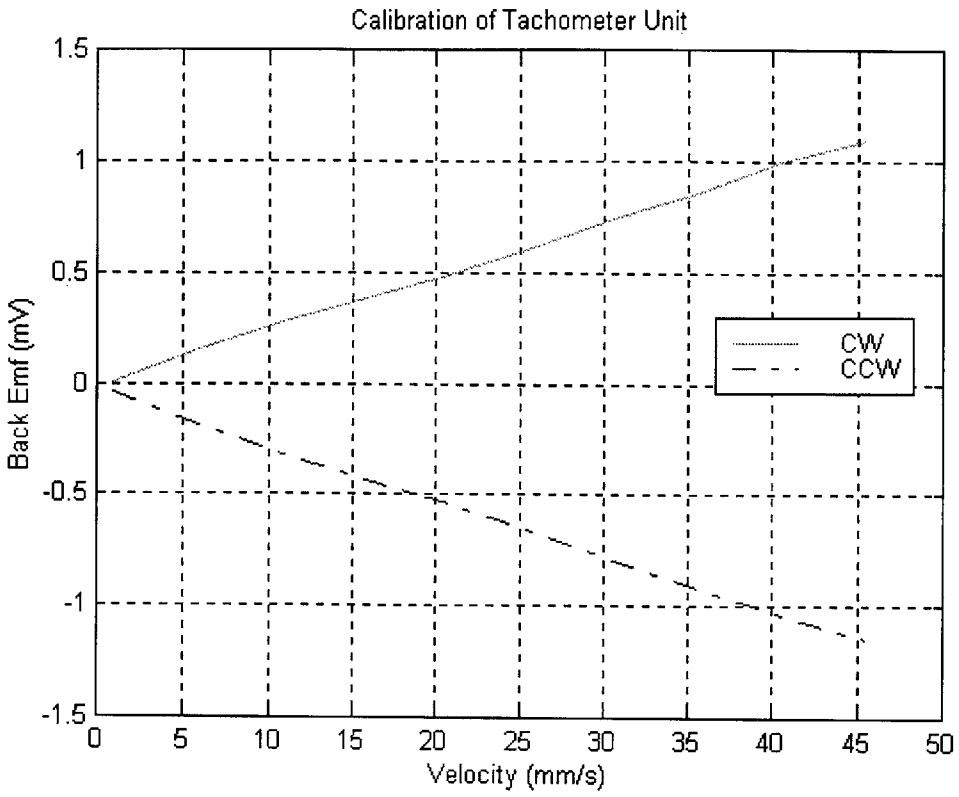

Figure 5.7 Tachometer calibration

5.5 Infrared-Based Velocity Sensor

Clinical physics and physiological measurement to investigate human dermis properties have utilized non-contact forms of thermal imaging. An external transducer is used to measure, indirectly, the effects of optical energy absorption within the tissue. Experiments to obtain thermograms of the patients' skin at the Tokyo Medical and Dentistry University utilized a thermovision camera and a mechanical system that provided a step change in ambient temperature [Togawa & Saito, 1994]. This data was then used to measure the emissivity of skin. Other tests conducted at Aberdeen Royal Hospital in Scotland measured the infrared emissivity of burn wounds in the wavelength range of 8-14 μm [Boylan et al, 1992]. The emissivity of normal skin was found to be approximately 0.966. Skin thermal properties are difficult to measure in vivo in steady state because there is a constant temperature gradient across the skin surface. However, thermographic measurements from stepwise changes in ambient temperature have shown that the thermal inertia of skin was scattered throughout a range of 1.4×10^3 to 2.1×10^3 $Ws^{1/2}m^{-2}K^{-1}$ [Huang & Togawa, 1995]. Pulsed photothermal radiometry uses an infrared detector to measure the blackbody infrared emissions at the tissue surface following an incident light pulse to measure the skin properties [Anderson et al, 1989].

The MIT/MI proposed detecting the in-vivo continuous infrared emission of a locally heated skin area as a means of developing a non-contact velocity sensor. A unit containing both a heat source and an infrared detector is to be moved along the surface of the skin. Figure 5.8 shows a heating element placed ¼ inch ahead of the detector. As the unit is moved with velocity V, the heated skin that was initially directly below the lamp will come within range of the detector after a certain time period.

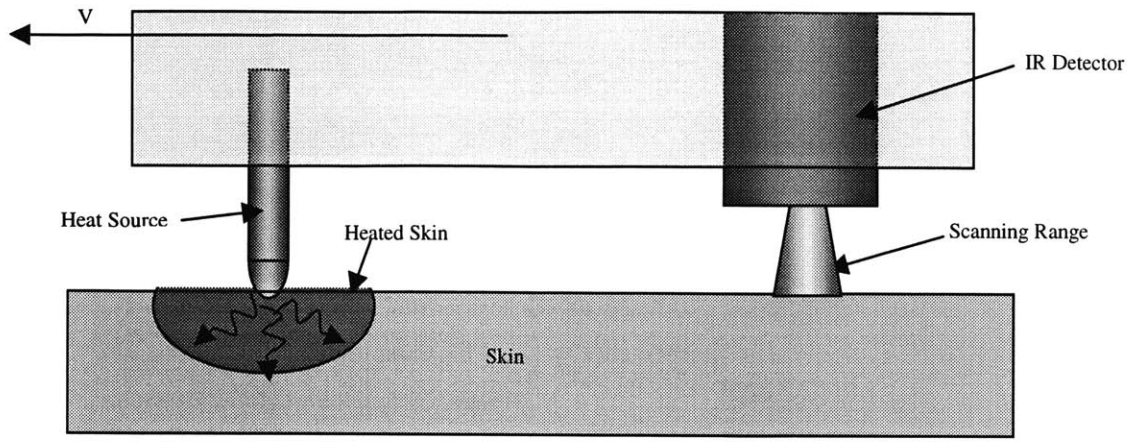

Figure 5.8 Diagram of proposed set-up of IR-based velocity sensor .

It was hypothesized that the infrared emission reading from the heated epidermis would vary, due to the thermal inertia of the skin, as the velocity of the unit is changed. Experiments would be conducted to investigate the relationship between velocity of unit and thermocouple output.

An Omega® OS36-E-140F series Infrared E-Thermocouple that is suitable for high emissivity surfaces was chosen. The spectral response ranged between 6.5 to14 μm, closely matching the emissivity range of Boylan et al. The thermocouple has an accuracy of +/-2% at its nominal linear range between 25 -80°C, 0.0001C resolution and a time response of 80 msecs. A 3mm wire-ended filament lamp of 0.3 W was used as the heat source. To detect a relative change of temperature, the thermocouple was connected directly to a Keithley Metrabyte® 12-bit DAQ (DAS801). A LabVIEW ® routine sampling at 100 Hz was used to analyze the data. The author's arm was placed on a linear belt of known velocity and passed under the stationary thermal sensor unit. Figure5.8 shows the unit with the IR sensor located at the center. The filament lamp and two

supporting legs form a three-point kinematic coupling to level the IR sensor at a fixed distance to the skin beneath.

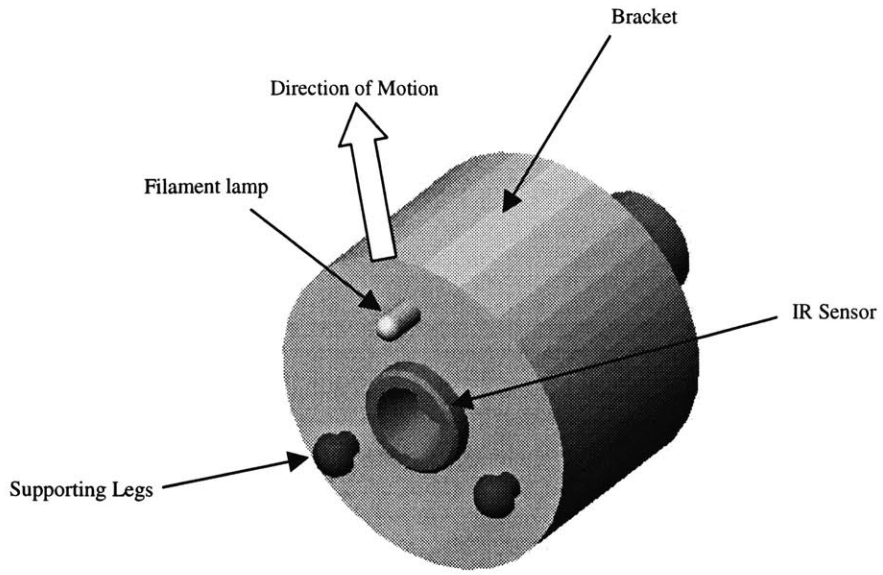

Figure 5.8 IR-sensor based velocity sensor unit

5.5.1 Experimental Results

The empirical results were inconclusive. This could be due to the existence of a large thermal gradient across the skin surface and varying temperatures from one point to another. This was observed in control experiments that were conducted without the heating element. The method of measuring the optical emissions of the skin relies on knowledge of the thermal and mechanical properties of the tissue, which are not always spatially uniform and constant. Skin is a turbid medium with slightly different optical properties from point to point. Environmental noise was another source of data error. Filters could not be implemented as the actual skin characteristics were not precisely known and there exist a possibility that pertinent data would be lost as a result.

As the unit speed is increase, the contact time of the filament lamp with the skin is shorter. This would in turn reduce the rise in temperature of the skin for the given lamp power output given a constant skin thermal inertia. However, the sensor would reach the heated surface quicker. The opposite holds for lower velocities. Due to the nature of the experiment, many of the test variables could not be controlled.

Figure 5.9 shows two experimental and control results each. Control experiments, where the heating element was not activated, were added to give a comparison in performance. The four experiments were conducted over the author's same forearm. There is no conclusive relationship between the velocity and thermocouple temperature. Further analysis would be required if this approach was to be pursued further.

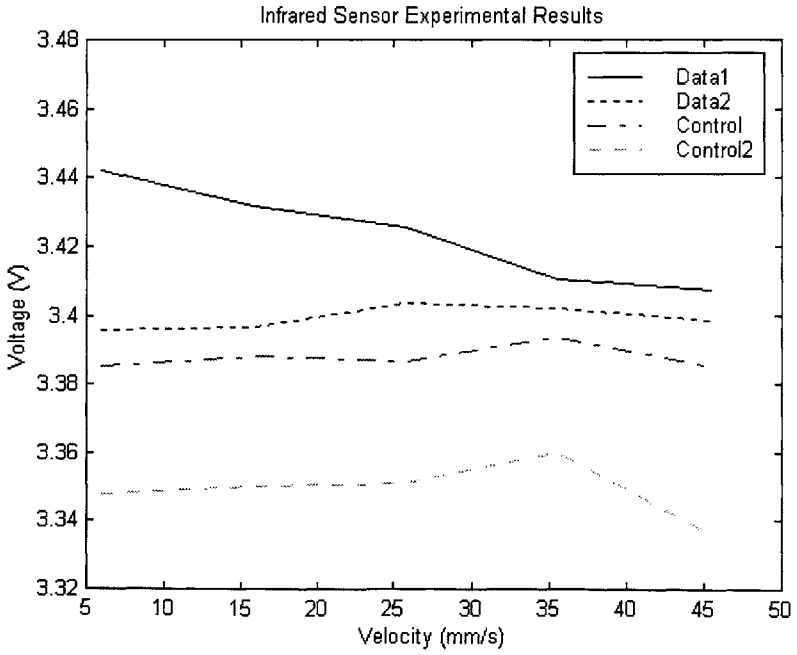

Figure 5.9 Infrared-sensor experimental results

5.6 Back Scattering Based Velocity Sensor

The study of light propagation in human tissue is central to many dermatological applications. The characteristic absorption and scattering of light determines its distribution within the tissue. In this section, the principles and the potential future application as a velocity sensor of optical reflectance of light in the 680-1000nm spectral region will be discussed.

At these wavelengths, the absorption of light is at a minimum in soft tissues. This region of relatively low absorption is often termed the 'therapeutic window'. From Figure 1.4 in chapter 1, it can be seen that shorter wavelength absorption is high due to hemoglobin and pigmentation such as melanin. At longer wavelengths, in the infrared region, the absorption by tissue water is high. The spectral range within the 'therapeutic window' allows substantial remittance of scattered light out of the tissue after relatively deep penetration. However, optical spectrum of light remitted from tissue is strongly affected by scattering and does not simply depend on the intrinsic absorption spectrum although it has a heavy influence. The scattering in tissues is due to discontinuities in refractive index on the microscopic level.

The MIT/MI investigated detecting the in-vivo continuous back scattering of light at wavelengths of 660nm and 980nm from the human skin as a method of sensing velocity. The experimental set-up, as shown in Figure 5.10, consist of a source fiber connected to a solid state light source placed at a separation distance (r) to a collector fiber coupled to a photodetector. Incident photons in a turbid medium undergo multiple scatterings before they reach the detector. The travelling direction of a photon changes randomly with each scattering occurrence. The collector and source fiber are connected

to a black delrin holder. The face of the holder with the exposed fiber tips is pressed firmly against the skin to reduce the diffuse reflectance from the surface of the skin. The black delrin holder absorbs any photon reflected off the skin near the emitter to reduce reading errors. In general, surface roughness decreases the specular reflectance and increases the diffuse reflectance. The separation of the source-detector is varied to investigate the performance of the emitter-detector unit. Cui et al questioned whether photons that migrate deeper should have longer path lengths for a given source-detector separation [Cui et al, 1991]. The path length was defined as the length of the travel trace of a photon that reaches the detector. Wilson and Jacques showed that for shallow penetration depth, the local diffuse reflectance had an inverse relation to the separation distance [Wilson & Jacques, 1990].

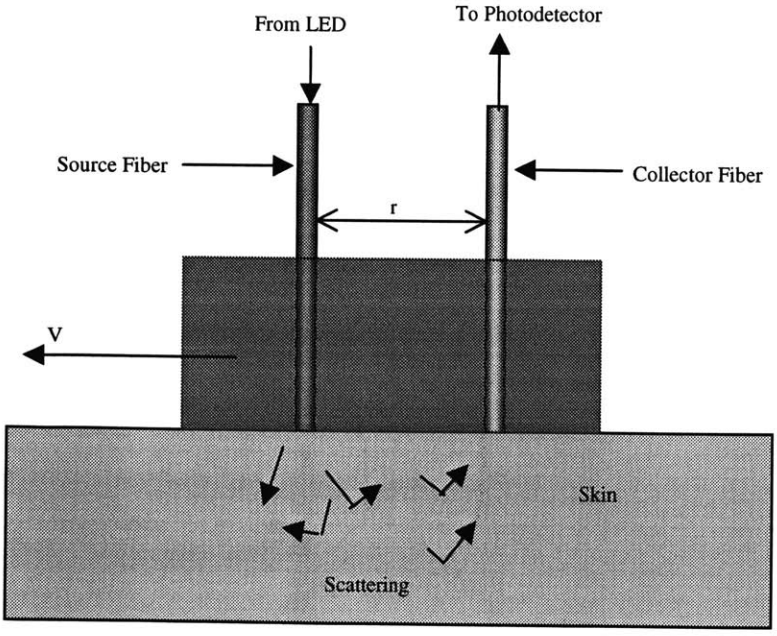

Figure 5.10 Diagram of experimental set-up

The experiments intend to investigate the normalized size of the discontinuities <Z> in the human skin. The hypothesis starts off with a simple assumption that with a given velocity and a known duration of a high signal, the size of the discontinuity can be found. A highly idealized scenario is illustrated in figure5.11. As the light source and detector unit moves with a known velocity (V) through a highly absorbing homogeneous medium, which contains only one discontinuity of unknown size (X), the photodetector will read a high signal for the duration (T) when the sensor is directly above the discontinuity. The size of the discontinuity (X) is the product of the velocity (V) and the time duration (T).

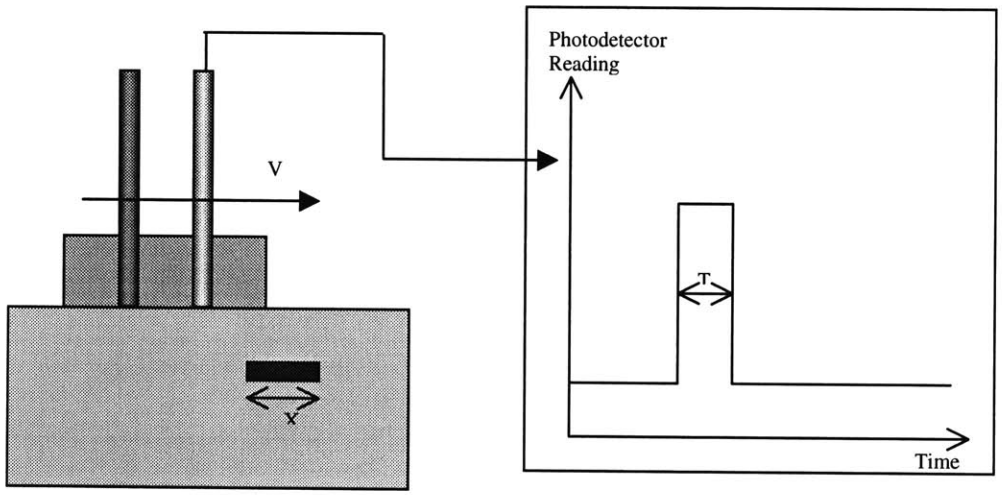

Figure 5.11 Data results from a highly idealised scenario

The skin is a heterogeneous medium with dynamic and different properties due to the distribution of discontinuities such as hemoglobin, melanin, aqueous –lipid membrane interfaces surrounding and within each cell and collagen fibrils within an extracellular matrix. Thus, the experiments will attempt to find the normalized dimension of the discontinuities <Z>. It is expected that the data from the photodetector would be highly

non-uniform with many jagged edges and troughs of varying amplitudes. To find the normalized time step, a routine will be written in Matlab® to analyze the normalized time <T> duration at which the voltage readings from the detector exceed a chosen threshold value. The program will also analyze the spectral power density of the data points. As the experiments are empirical, the Root Mean Square (RMS) of the data points is chosen as the threshold value. This value was chosen because RMS is generally used for equipment voltage and current ratings and error deviations. For data points that fall between the RMS value, a first order curve fit to extrapolate and solve the corresponding time value will be performed by the Matlab® routine. Figure 5.12 shows a typical jagged response expected at a given velocity, V.

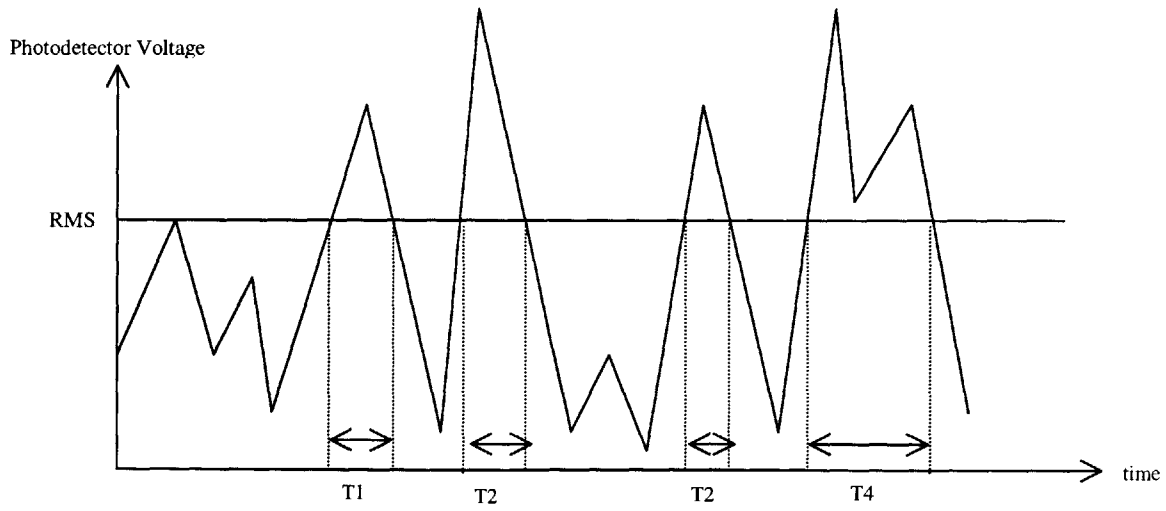

Figure 5.12 Jagged expected response from photodetector

Normalized time <T> can be found using:

$$< T >= \frac{\sum_{1}^{n} T_n}{n}$$

The normalized discontinuity dimension <Z> that should remain constant for any given skin: $\langle Z \rangle = V \times \langle T \rangle$

Unlike the IR-based velocity sensing strategy that measured the secondary effect of energy absorption, this methods offers more advantages. The measurement does not depend on the thermal properties of the tissue, it is non-invasive and may have depth profiling or localization capability.

For the near infrared 980nm wavelength experimental set-up, a Siemens SFH450V LED emitter and a Siemens SFH 250V PIN photodetector were used. The emitter has a peak wavelength of 950nm, spectral bandwidth of 55nm and power dissipation of 0.2W. The plastic fiber optic photodiode has maximum photosensitivity at 850nm and a spectral range of 400nm to 1100nm. Silicon photodetectors were chosen over germanium because of their maximum sensitivity in the near infrared region. The emitter and detector are connected to 1 mm polymer fiber optic cables via screw mounts.

The red wavelength system of 660nm composed of a Fibre Data emitter (H22E-200BHR) with peak emission wavelength at 660nm and power output of approximately 0.1W. The PIN photodetector used is a Fibre Data (H22R-8801IR) with peak responsiveness at 850nm and a spectral range of 400-1100nm. The emitters and detectors are connected to 1mm polymer optical fiber with SMA mounting style.

The LED emitters and photodetectors are used for measurement under steady state conditions using continuos (CW) irradiation. A schematic of the electrical set-up is given in Figure 5.13. The voltage drop across the resistor in the photodetector circuit was connected to a 16-bit National Instruments® DAQ (ATMIO 16XE50) sampling at 100 Hz

through a LabVIEW® routine. The photodiode is in the photoconductive mode; the p-n junction is operated with reverse bias. At high enough reverse voltage, a current will flow. As the light intensity increases, the voltage across the Rl increases proportionally. Back-biasing a photovoltaic detector will enable the detector to respond better to weak and rapidly varying optical signals.

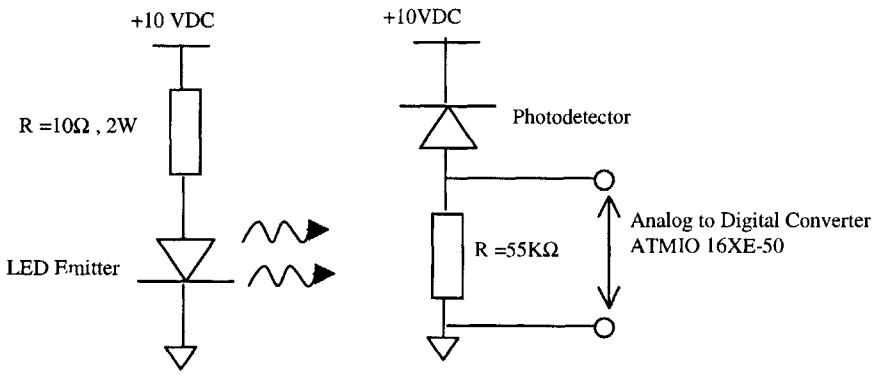

Figure 5.13 Electrical schematic of LED and photodetector circuit.

5.6.1 Experimental results

As the separation (r) was decreased, the overall scattering signal increased. This agrees with the data from Wilson and Jacques that showed an inverse relationship between diffuse reflectance and separation distance. However, the experimental results relating to the velocity of the source-detector unit and the normalized time of the sampled data were inconclusive and provided no observable trend. The spectral analysis also yielded no direct observable trend at the various velocities. It was expected that the normalized time would decrease as the velocity is increased, assuming that the normalized dimension of the discontinuities remains constant, which should be the case given the same test subject. The experiments were performed on the author's right forearm to maintain consistency. The experimental test results for the 660nm and 980nm experiments are shown in Figures 5.14 and 5.15.

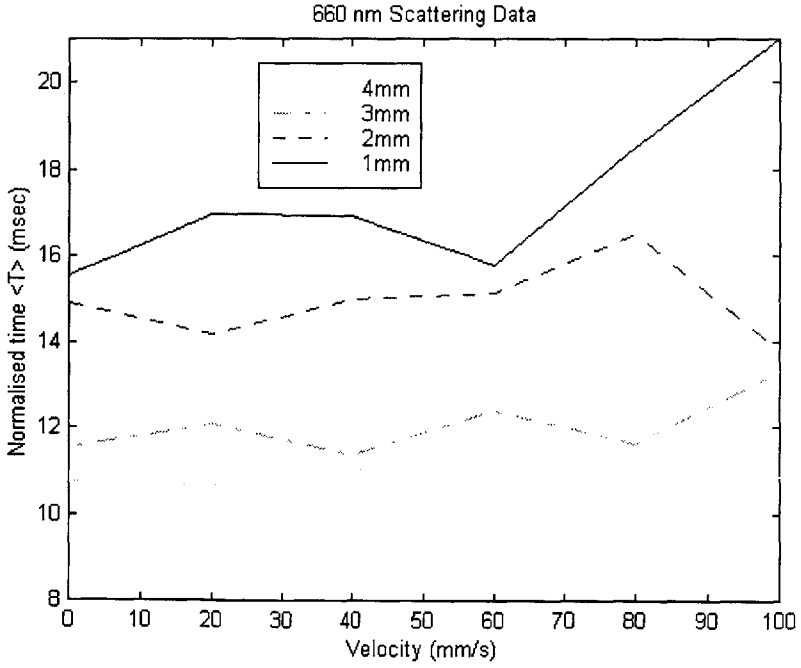

Figure 5.14 660nm scattering data

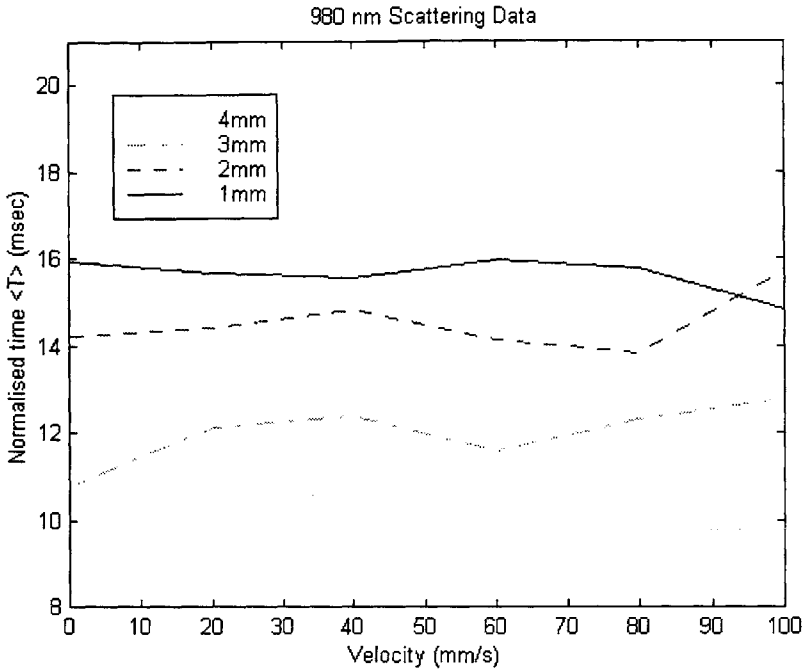

Figure 5.15 980 scattering data

The spectral characteristics of diffuse remittance from tissue is a complex function comprising of variables such as scattering and absorption which in turn depend also on the distribution of chromophores and scattering components, together with the source-tissue-detector interaction. Thus, the metabolic, physiologic and structural characteristics of the tissue produce the intrinsic scattering properties of the tissue, which in turn produce the measured observable parameters. If a normalized discontinuity dimension can be found, another challenge remains in solving the inverse problem and in so, deriving the velocity of the unit for a given skin type. A bigger challenge would lie in the ability to create a robust algorithm that will be able to accommodate different skin types and have a quick response time.

It is proposed that a time-resolved measurement approach would increase the sensitivity of the set-up. A pulse generator of a fixed frequency could be connected to the LED with a matching frequency sampling rate at the detector. Consequently, an alternative light source of higher power could also be used to increase the penetration characteristic of the system. No publications were found that could provide proper power rating for optimal epidermal light scattering.

6 Conclusion

6.1 MIT/MI Automated Precision Scanner

Clinical trials of the MIT/MI Scanner interfaced with the E2000^{TM} system have shown an increase in process throughput. On average, the scanner is capable of covering an area of 4.5 inch^2 in approximately one minute. The scan rate varies with the different types of laser-skin interactions. This occurs because the scanner controller relies on the laser trigger pulse to advance to the next step. A laser treatment on a patient's back (18 inches by 20 inches) using the 10mm hexagon tip that would have normally taken 4-6 hours with the manual operation [Garden City Epilaser, 1998], can potentially be reduced to 80 minutes with the scanner.

In addition, the full manual procedure on the back cannot be performed in one seating as the tedious operation leads to operator fatigue. This also leads to positional and application force errors. The advantage of the automated scanner is its ability to maintain process speed, consistency and uniformity even at long operation hours. The scanner received positive feedback from the providers as it relieved them from the tedious and laborious routine.

In the clinical tests performed at the Department of Photomedicine at the Wellman Laboratories of Massachusetts General Hospital (MGH), the scanner was tested on a few patches of a patient's back. Figure 6.1 shows MGH staff performing the laser procedure on a patient. A white Caucasian male of age 35, with Fitzpatrick II skin type and brown hair was treated on the back at the maximum fluence of 50 J/cm^2. The scan rate averaged two minutes for a three-inch square area and had a repeated cycle rate of

25%. At maximum fluence, the tip is super-cooled to minus 10°C, and this causes the moisture on the skin surface to stick to the sapphire tip, preventing proper contact conditions. To overcome this limitation, the Z-axis should be lengthened to allow more travel to achieve good separation between the skin and laser tip.

Another test conducted on the lower thigh of a volunteer at Palomar Medical laboratories showed a significantly improved scan rate. A white Caucasian male of age 33, with Fitzpatrick II skin type and brown hair was treated at a minimum fluence of 10 J/cm^2. The average time taken to treat a three inch square area was approximately one minute. The faster scan rate was also due to the lower repeated cycle rate of 5%.

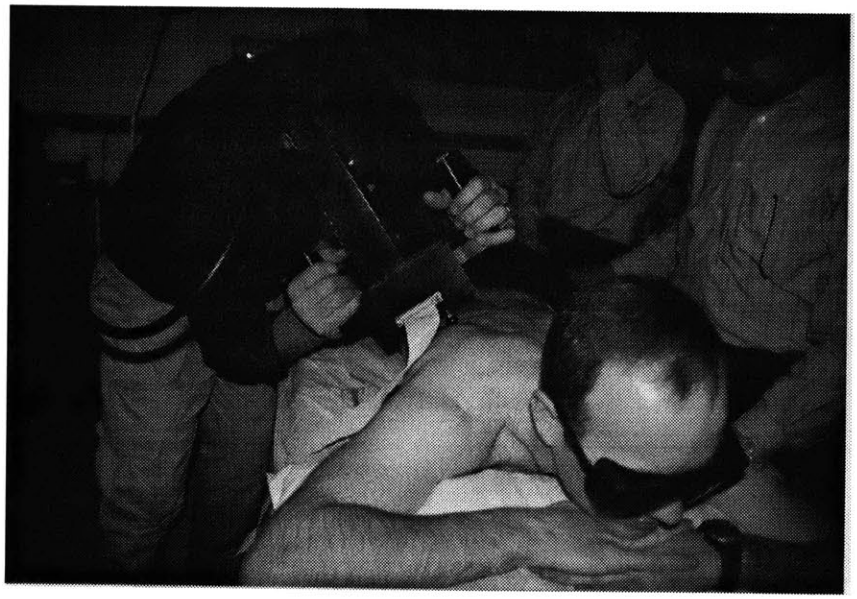

Figure 6.6.1 Clinical test of the laser-scanner system conducted on a patient at MGH

The controlled applied force increases patient comfort and provides better surface results. The force can be easily changed through the user interface to suit different patients. Gross overlapping is a major drawback with the manual process. This uncontrolled overlapping leads to burning of the skin and poor time performance. Another problem with the small laser tip size is the lack of visual cues to show treated areas. Currently, the operator looks for regions of inflamed skin, compression outlines of the spots left on the skin surface by the hexagonal tip and singed hair as visual cues of treated areas. These methods are unreliable and lead to consistency and uniformity problems. The scan areas can be easily adjusted through the user interface to cover different grid areas with various step sizes. Figure 6.2 shows the rectangular laser treated areas with consistent and uniform results. There are no unfired spots within the scan area. These marks disappear in a few minutes.

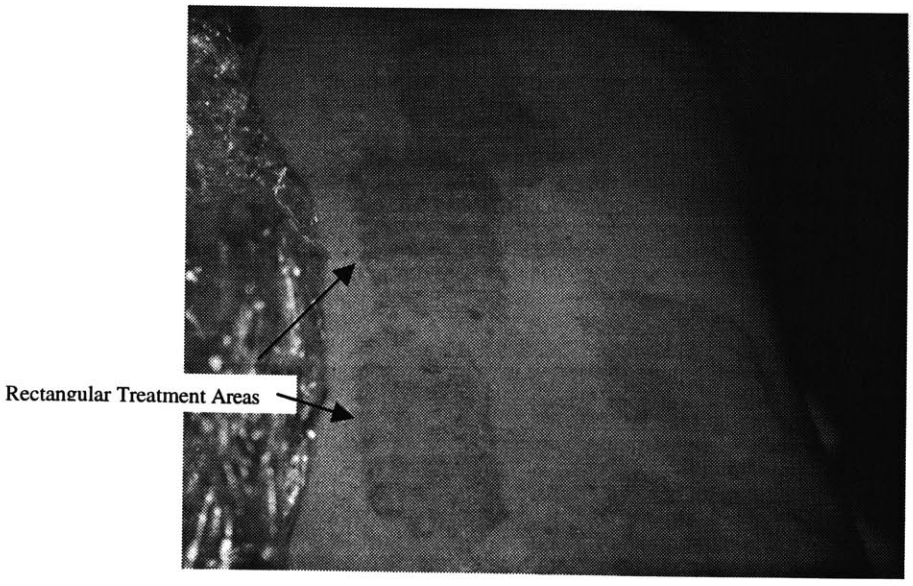

Figure 6.6.2 Consistent and uniform rectangular scan areas on patient's back

The X and Y stages were driven at varying step sizes to find the optimum scan pattern. The tests were performed on a laser-light sensitive Zap-It® paper. The left, center and right grid patterns in Figure 6.3 were performed with 6mm, 7mm and 8mm step separations on the X and Y axes, respectively. The pattern formed by the 6mm steps was compact with gross overlapping leaving no unfired regions. The 8mm steps had minimal overlapping with significant missed spot regions due to the hexagonal-shaped laser tip.

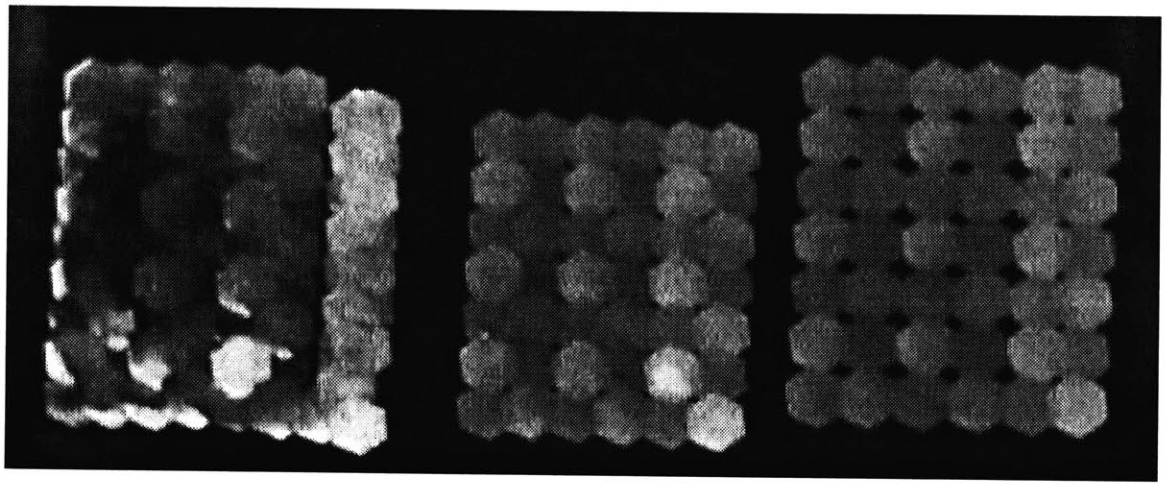

Figure 6.3 Scan patterns with varying step sizes. (L-R) 6mm, 7mm and 8mm step sizes

This preliminary test indicated that a step size between 6 mm and 7mm would provide the optimum scan pattern. This was achieved when the step size was set at 6.75mm. The left and right scan patterns in Figure 6.4 were formed by 6.5 mm and 6.75 mm step separations, respectively. The 6.75 mm scan pattern provided the optimum trade-off between overlapping and missed spots. The consistent scan pattern forms one of the major advantages of the automated scanner. It is difficult to achieve such consistency with the manual procedure.

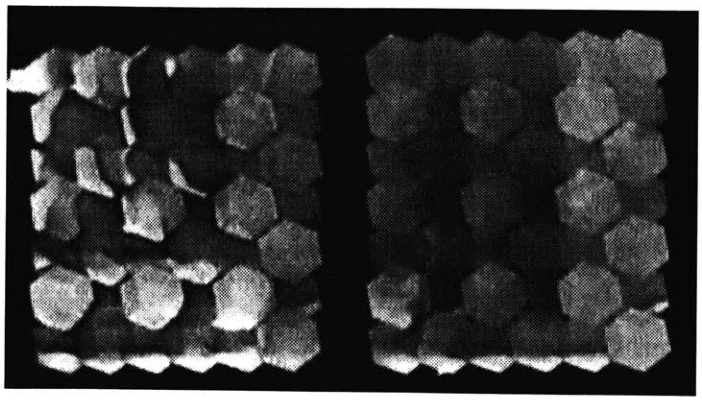

Figure 6.4 Scan patterns from varying step sizes. (L,R) 6.5mm and 6.75mm

Clinical tests indicated that a flattened skin surface is ideal for optimal laser-skin interaction. The four-ball discrete contact base was replaced by a flat ring-like surface. This circular base exerts a uniform force on the skin surface and flattens the treatment area, making the skin tighter and more manageable. This has another added advantage of increasing the travel length of the Z-axis. The new base has a grid pattern outline to facilitate proper placement of the scanner in the succeeding scan area. This would ensure that the scan grids lie adjacent to one another without any missed spots in between. The new base and outline grid can be seen in Figure 6.5 and Figure 6.6.

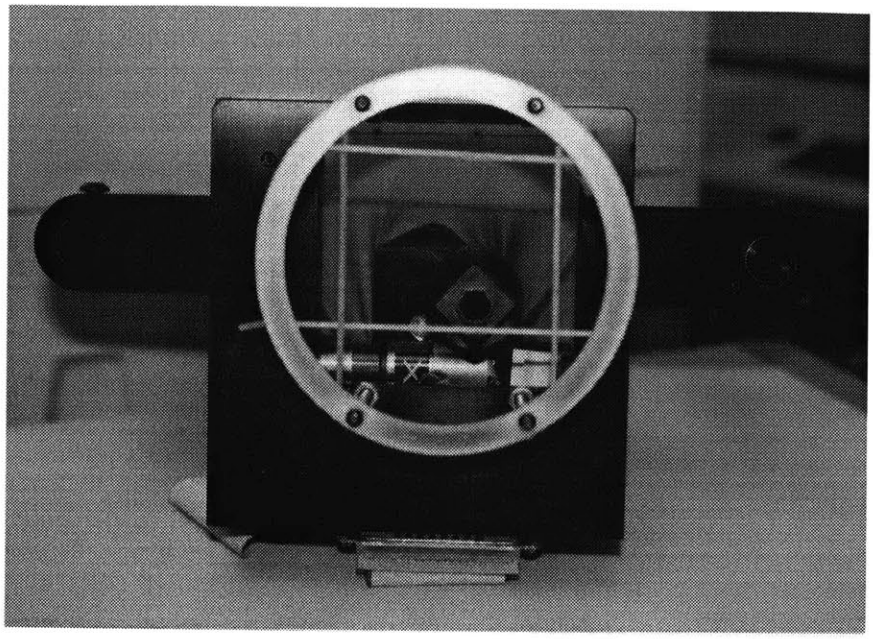

Figure 6.5Bottom view of the scanner showing the new circular base

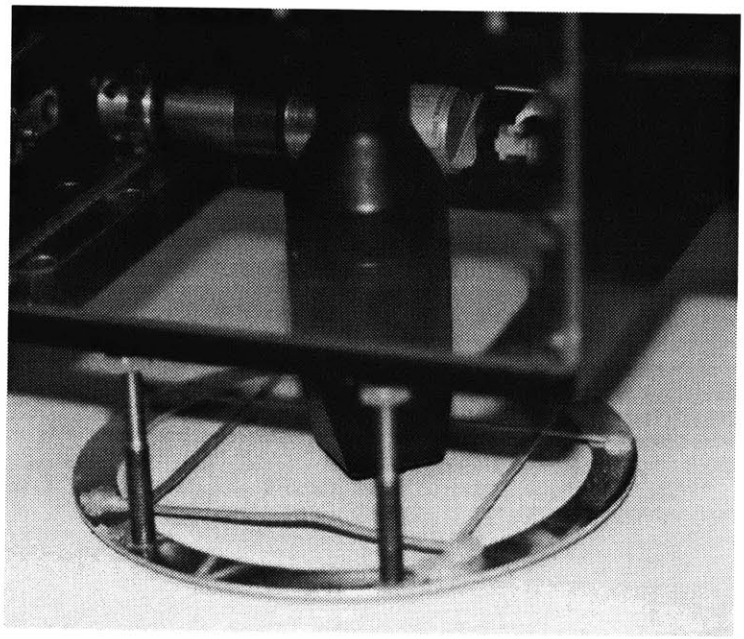

Figure 6.6 Outline markings on the circular base to help scanner positioning

The scanner was found to work well on level skin surfaces with minimum curvature. Curved surfaces pose a challenge as the EpiWand® contacts the skin at an oblique angle. When this happens and the laser does not pulse within half a second, the scanner would repeat the same cycle until optimum conditions for laser initiation is achieved. Test trials performed on the knee, which has a high curvature, produced approximately 10% repeated cycle. Most repeated cycles produced successful contact firing by the second try. A proposed improvement to the production scanner would be the addition of a rotational joint on the hand-piece carrier. This would ensure that the laser hand piece contacts the skin perpendicularly regardless of the curvature.

Tests have also shown that altering the scan pattern can enhance the treatment procedure. The current method rasters the laser hand-piece in the X and Y directions as illustrated in Figure 6.7.

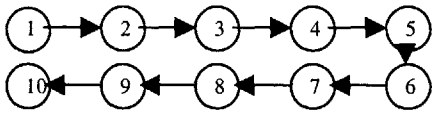

Figure 6.7 Raster scan pattern of the X and Y axes

Figure 6.8 illustrates an alternative 'Zig-Zag' pattern that helped improve cooling time of the laser tip between treatment spots. This will also reduce thermal damage to the skin as the laser energy is distributed more evenly. Tests performed showed that the marginally longer travel lengths lead to a negligible time increase. There would be realignment issues with the 'Zig-Zag' pattern if the scanner were removed during the laser process. The user interface allows the operator to toggle between the two different scan patterns.

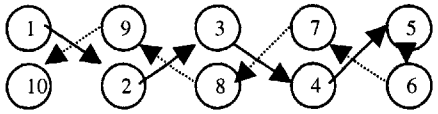

Figure 6.8 Zig-Zag scan pattern of the X and Y axes

The modified scanner with the flat circular base and 'Zig-Zag' scan pattern, set at 6.75 mm separations, showed an improved treatment rate when tested on a volunteer in clinical trials performed at MGH. A mid-forty white Caucasian male with Fitzpatrick II skin and brown hair was treated on sections of his back at a fluence of 40 J/cm^2. The new base design provided adequate clearance between the skin and laser tip in the Z-axis at the end of each successful laser fire. The scanner averaged one minute for a three square inches treatment area with a 5% repeated cycle rate.

6.2 Velocity Sensor

The miniature tachometer (Figure 6.7) provides the best performance given its size. The system is robust, compact and was shown to meet all design specifications. The only limitation of the tachometer system is the mechanical contact between the wheel and the skin, which raises maintenance issues. This initiated the development of two non-contact optical based velocity sensors: the absorption/emission and the light scattering approaches. Although similar general set-ups have been used in tissue optical property studies, no publications have been found that used either method as a means of detecting velocity. Skin is a complex, highly dynamic and multi-layered optical medium, and the experiments were conducted to investigate the possibilities of correlating scattering and emissivity data to velocity. Although the experimental results were inconclusive, future research work in this field adopting different methodologies and equipment, might yield beneficial data. Further analysis would be required if either approach were to be pursued further.

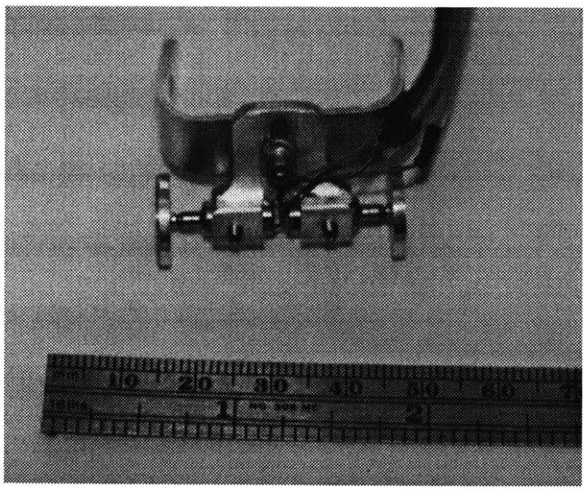

Figure 6.7 Miniature tachometer

References

1. Trost D.MS, Zacherl A. RN, Smith M. MD, "Surgical laser properties and their tissue interaction," Chapter12, Mosby-Year Book, Inc., 1992.
2. Moretti M., Miller I. PhD, "Laser assisted hair removal: A technology/market study," Medical Insight, Inc., Version1.2, June 1996.
3. Moretti M., "Medical laser insight: Business opportunities and market analysis," Vol.4, No.7, July 1996.
4. Wheeland R. MD, "Laser assisted hair removal," Lasers in Dermatology, Vol. 15, No.3, pp. 467-477, July 1997.
5. Clark P., "Light and laser hair removal," Aesthetic Surgical Journal, pp. 65-67, Jan/Feb 1998.
6. Grossman M., Dietricx C., Farinelli W., Flotte T., Anderson R., "Damage to hair follicles by normal-mode ruby laser pulses. Clinical and Laboratory Studies," Journal of the American Academy of Dermatology, pp. 889-894, Dec 1996.
7. Altschuler G., Zenzie H., "Contact cooling of skin," Palomar Medical Products, Inc., Feb 1998.
8. Muller G., Schaldach B., "Safety and Laser Tissue Interaction," Advances in Laser Medicine II. Freie Universitat Berlin/The International Society for Optical Engineers, Vol.1143, 1989.
9. Katzir A., "Lasers and Optical Fibers in Medicine," Academic Press, 1993.
10. Carruth J., McKenzie A., "Medical Lasers. Science and clinical practice," Adam Hilger Ltd., 1986.

11. David B., "Therapeutic Lasers. Theory and Practice," Churchill Livingstone, 1994.

12. Ogata K., "Modern Control Engineering. 3rd Edition," Prentice-Hall, 1997.

13. Slocum A., "Precision Machine Design," Society of Manufacturing Engineers, 1992.

14. Boylan A., Martin C.J., Gardner C.G., "Infrared emmisivity of burn wounds," Clinical Physics and Physiological Measurement, Vol.13, No.2, pp.125-127, May 1992.

15. Huang J., Togawa T., "Measurement of the thermal inertia of the skin using successive thermograms taken at a stepwise change in ambient radiation temperature," Physiological Measurement, Vol.16, No.4, pp. 213-225, Nov 1995.

16. Togawa T., Saito H., "Noncontact imaging of thermal-properties of the skin," Physiological Measurement, Vol.15, No.3, pp. 291-298, Aug 1994.

17. Cui W., Wang N., Chance B., "Study of photon migration depths with time-resolved spectroscopy," Optics Letters, Vol.16, No.21, pp. 1632-1634, Nov 1991.

18. Wilson B., Jacques S., "Optical reflectance and transmittance of tissue: Principle and applications," IEEE Journal of Quantum Electronics, Vol.26, No.12, Dec 1990.

19. Anderson R., Beck H., Bruggemann U., Farinelli W., Jacques S., Parrish J., "Pulse photothermal radiometry in turbid media: Internal reflection of backscattering radiation strongly influences optical dosimetry," Appl. Opt., Vol.28, pp. 2256-2262, 1989.

20. Ball Screws and Actuators Co. (BSA), Catalog No. 93-2, pp.50, 1992.

21. Garden City Epilaser, http://www.tpisaledays.com/gardencity/lasercenter.html, June 1998